


LOTUS: A (non-)LTE Optimization Tool for Uniform derivation of Stellar atmospheric parameters

YANGYANG LI(李扬洋) ¹ AND RANA EZZEDDINE ^{1,2}



¹*Department of Astronomy, University of Florida, Bryant Space Science Center, Gainesville, FL 32611, USA*

²*Joint Institute for Nuclear Astrophysics - Center for Evolution of the Elements, USA*

(Received July 20, 2022; Revised XX XX, XXXX; Accepted XX XX, XXXX)

Submitted to AJ

ABSTRACT

Precise fundamental atmospheric stellar parameters and abundance determination of individual elements in stars are important for all stellar population studies. Non-Local Thermodynamic Equilibrium (Non-LTE; hereafter NLTE) models are often important for such high precision, however, can be computationally complex and expensive, which renders the models less utilized in spectroscopic analyses. To alleviate the computational burden of such models, we developed a robust 1D, LTE and NLTE fundamental atmospheric stellar parameter derivation tool, LOTUS, to determine the effective temperature T_{eff} , surface gravity $\log g$, metallicity $[\text{Fe}/\text{H}]$ and microturbulent velocity v_{mic} for FGK type stars, from equivalent width (EW) measurements of Fe I and Fe II lines. We utilize a generalized curve of growth method to take into account the EW dependencies of each Fe I and Fe II line on the corresponding atmospheric stellar parameters. A global differential evolution optimization algorithm is then used to derive the optimized fundamental parameters. Additionally, LOTUS can determine precise uncertainties for each stellar parameter using a Markov Chain Monte Carlo (MCMC) algorithm. We test and apply LOTUS on a sample of benchmark stars, as well as stars with available asteroseismic surface gravities from the K2 survey, and metal-poor stars from *R*-process Alliance (RPA) survey. We find very good agreement between our NLTE-derived parameters in LOTUS to non-spectroscopic values within $T_{\text{eff}} = \pm 30$ K and $\log g = \pm 0.20$ dex for benchmark stars. We provide open access of our code, as well as of the interpolated pre-computed NLTE EW grids available on Github , and documentation with working examples on Readthedocs .

Keywords: Astronomical techniques (1684), Spectroscopy (1558); Stellar atmospheres (1584), Stellar physics (1621), Stellar photospheres (1237); Fundamental

parameters of stars (555), Astrometry (80), Effective temperature (449), Surface gravity (1669), Metallicity (1031)

1. INTRODUCTION

Precise characterization of stellar spectra is a key ingredient for understanding several fields of modern astrophysics, including the physical and chemical properties and abundances of stars (Asplund et al. 2009; Jofré et al. 2019), galactic formation and evolution (Audouze & Tinsley 1976; McWilliam 1997; Kobayashi et al. 2006), as well as macro and micro physical phenomena near the surface of stars (Miesch & Toomre 2009; Linsky 2017). This accurate level of characterization is also needed for the detection of extra-solar planets when using radial velocity methods (Vanderburg et al. 2016).

With the current inflow of stellar spectra from ongoing and future large observational spectroscopic surveys including, SDSS-V (Kollmeier et al. 2017, $R \sim 2000$ and ~ 22500), LAMOST (Liu et al. 2020, $R \sim 7500$; Cui et al. 2012; Zhao et al. 2012; Deng et al. 2012, $R \sim 1800$), APOGEE (Ahumada et al. 2020, $R \sim 22500$), RAVE (Steinmetz et al. 2020, $R \sim 7500$), GALAH (De Silva et al. 2015, $R \sim 28000$), as well as the upcoming WEAVE (Dalton et al. 2016, $R \sim 5000$ and $R \sim 20000$), 4MOST (de Jong et al. 2019, $R \sim 20000$) and PLATO (Miglio et al. 2017), stellar spectroscopy will be providing $\sim 10^5$ of golden opportunities to study the chemical and dynamical properties of stars in the Galaxy to help understand its build-up history and evolution.

Atmospheric fundamental stellar parameters, including T_{eff} , $\log g$, $[\text{Fe}/\text{H}]$ and micro-turbulence velocity v_{mic} , as well as chemical abundances of stars, are determined from the observed spectra of a given star by fitting theoretical synthetic spectra based on assumptions of geometric structures (1D versus 3D), radiative transfer assumptions (Local Thermodynamic Equilibrium; hereafter LTE, versus Non-

Local Thermodynamic Equilibrium; hereafter NLTE). Two classical methods are commonly used to derive stellar atmospheric parameters from stellar spectra: either 1) by iteratively fitting the observed spectra to synthetic spectral models until a best-fit match is met at the corresponding stellar parameters, or 2) by measuring chemical abundances of Fe I and Fe II lines from equivalent widths (EW) measurements, and employing optimization of excitation and ionization equilibrium by changing the stellar parameters iteratively until trends with excitation potential energies (χ) and reduced equivalent widths ($\log(EW/\lambda)$) of the lines are minimized.

While the former method of spectral synthesis might outperform the latter in crowded spectral regions or spectra dominated by strong lines ($\log(EW/\lambda) > -4.5$), the EW method generally requires less calculation time and resources than synthetic spectra, making it a simpler and more widely applied tool to measure atmospheric stellar atmospheric parameters and chemical abundances. Classical radiative transfer models for deriving stellar parameters and chemical abundances from observed spectra assume LTE. Under LTE, the gas and chemical particles throughout the stellar atmosphere satisfy the Saha-Boltzmann excitation and ionization balance equations. Several stellar atmospheric parameter tools implementing classical 1D and LTE approximations for spectroscopic analyses already exist and are widely used (e.g., MATISSE (Recio-Blanco et al. 2006), MyGIsFOS (Sbordone et al. 2014), the APOGEE pipeline ASCAP (García Pérez et al. 2016), GALA (Mucciarelli et al. 2013), DOOp (Cantat-Gaudin et al. 2014), ARES (Sousa et al. 2015), StePar (Tabernero et al. 2019), and FASMA (Tsantaki & Andreasen 2021) using the EW method).

The LTE assumption utilized by all of these tools is, however, not physically motivated when applied to evolved giants and/or metal-poor stars (Lind et al. 2012; Ezzeddine et al. 2017; Mashonkina et al. 2017; Amarsi et al. 2020). Inelastic collisional interactions between atoms and electrons or neutral hydrogen in the atmospheres of cool stars usually drive the local conditions in these atmospheres towards LTE. In metal-poor and giant stars, limited electron donors from metals are not able to induce enough collisions to maintain collisional equilibrium in the line-forming regions (Hubeny & Mihalas 2014), which drive line formation away from LTE (Mihalas & Athay 1973; Bergemann et al. 2012). Quantified deviations in abundances and stellar atmospheric parameters from LTE are commonly known as NLTE effects (Asplund 2005), which are mainly driven by deviations from statistical equilibrium or kinematic equilibrium.

To the authors’ current knowledge, the only stellar atmospheric and chemical abundance code taking NLTE effects into account is PySME (Wehrhahn 2021). It is based on the spectroscopic analysis code Spectroscopy Made Easy (SME; Piskunov & Valenti 2017), which has the capability to synthesize NLTE spectra of individual spectral lines. It can become tedious and time demanding to apply for a line-by-line stellar parameter determination. Therefore, a code that can automatically derive stellar parameters using EW is much needed, which is the main motivation of this paper as explained in more detail in the following sections.

In this work, we present a fast, automatic and robust spectroscopic analysis tool, LOTUS, which stands for a NLTE Optimization Tool Utilized for the derivation of atmospheric Stellar parameters, which allows the derivation of T_{eff} , $\log g$, $[\text{Fe}/\text{H}]$ and v_{mic} based on input EW measurements of Fe I and Fe II lines from stellar spectra. Either or both LTE and NLTE modes

can be chosen for the benefit of comparisons. As compared to traditional model-by-model full NLTE calculations, LOTUS can shorten the time of the determination of stellar parameters in NLTE assumption from several hours or even days (Hauschildt et al. 1997) to $\sim 15 - 30$ mins for each star. A Monte-Carlo Markov Chain (MCMC) analysis is also implemented to precisely estimate the uncertainties of the derived parameters. We test and apply our code on several benchmark stars, and stellar surveys with available non-spectroscopic atmospheric parameters for comparison and validation of our results.

The rest of the paper is organized as follows: In Section 2, we present a detailed description of LOTUS, and describe the input models for our NLTE calculations, as well as a description of the different modules of the code. In Section 3, we test our code and apply it to derive and compare the derived parameters of benchmark stars, and stars with non-spectroscopic derived parameters. In Section 4, we apply the code to a large sample of metal-poor stars and discuss the NLTE effects obtained via LOTUS. In Section 5, we present a discussion on the caveats and limitations of the code, and finally, in Section 6 we present a summary of our results and conclude.

2. DESCRIPTION OF LOTUS

LOTUS is designed to derive the fundamental atmospheric stellar parameters, namely, effective temperature (T_{eff}), surface gravity ($\log g$), metallicity ($[\text{Fe}/\text{H}]$) and microturbulent velocity (v_{mic}) of FGK type stars, by implementing observed measurements of equivalent widths (EW) for Fe I and Fe II lines as input. An example of a user input EW linelist is shown in Listing 1 below. The transition wavelength `obs_wavelength` (in Å), element and ionization stage (Fe I or Fe II), measured EW `obs_ew` (in mÅ) and excitation potential energy EP (in eV) are required.

```
1 obs_wavelength , element , obs_ew , obs_ep
```

```

2 4787.8266 , FeI , 44.2 , 3.00
3 4788.7566 , FeI , 65.5 , 3.24
4 4789.6508 , FeI , 83.3 , 3.55
5 6456.3796 , FeII , 59.2 , 3.9
6 . . .

```

Listing 1. Example of an input file format of observed EW measurements for FeI and FeII lines provided by users for LOTUS. `obs_wavelength` are in Å, `obs_ew` in mÅ, and `obs_ep` in eV.

LOTUS’s general modes of functionality are as follows: (i) Fe I and Fe II abundances are derived by interpolating a generalized curve of growth (GCOG) for each line in a pre-computed grid of theoretical EW in both LTE and NLTE, following the work done by [Boeche & Grebel \(2016\)](#). (ii) The stellar parameters are then derived by minimizing the slopes for excitation and ionization equilibrium, iteratively using a global minimization module. Finally, (iii) uncertainties of the derived atmospheric parameters are estimated utilizing a Markov Chain Monte Carlo (MCMC) algorithm. We describe each of these modules in detail in sub-section 2.2 below, after listing the input and radiative transfer models used in Section 2.1.

2.1. Input Models

2.1.1. Stellar Atmosphere Models

LOTUS incorporates 1D, LTE MARCS stellar atmospheric models ([Gustafsson et al. 1975, 2008](#)), covering a wide range of stellar parameters typical for FGK stars. Spherical atmospheric models were used for $\log g < 3.5$, otherwise, plane-parallel models were adopted. The grid of MARCS model atmosphere available online¹ offer reasonable coverage for the stellar parameters, however they exhibit wide gaps in effective temperature (steps of ~ 250 K), surface gravity (steps of ~ 0.5 cgs), and metallicity (steps of $\sim 0.25 - 0.50$ dex) to optimally explore the parameter space. We utilize the MARCS in-

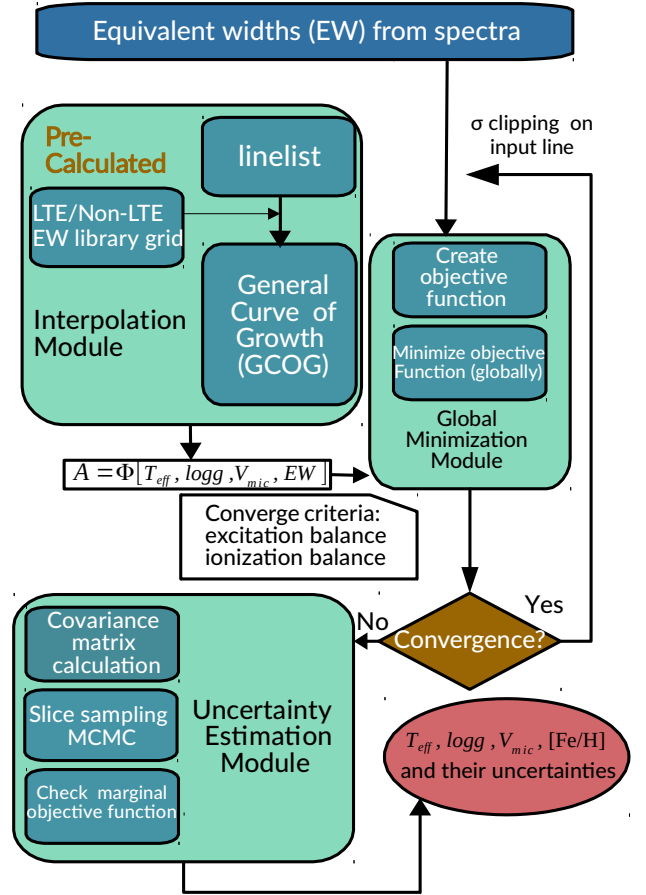


Figure 1. A flow diagram describing the working modules of LOTUS. Three main modules are used to derive the stellar parameters and their uncertainties: (i) An interpolation Module, (ii) a Global Minimization Module, and (iii) an Uncertainty Estimation Module. Input includes EW measurements of FeI and FeII of the absorption lines measured in the spectra. Users can define the number of σ clipping required to remove outliers (see Section 2.4.3 for details). Additionally, a halt condition for the value of the smallest allowable minimization function threshold can also be defined by users (see Section 2.4.3 for details).

terpolation subroutine `iterpol_marcs.f`² written by Thomas Masseron, to produce a higher resolution grid, with our final parameter grid ranging from 4000 K to 6850 K for T_{eff} (steps of 50 K), $\log g$ from 0.0 to 5.0 (steps of 0.1), $[\text{Fe}/\text{H}]$

¹ <https://marcs.astro.uu.se/>

² <http://marcs.astro.uu.se/software.php>

from -3.5 to $+0.5$ (steps of 0.5) and v_{mic} from 0.5 to 3.0 km s^{-1} (steps of 0.5 km s^{-1}).

2.1.2. Iron Model Atom

Computing theoretical NLTE Fe I and Fe II EWs requires the input of a comprehensive iron model with up-to-date radiative and collisional atomic data. For our EW grid calculations, we adopt a well-tested Fe I/Fe II model atom containing 846 Fe I and 1027 Fe II lines Ezzeddine et al. (2016, 2017, 2020). The atom includes absorption line transitions spanning the near-UV to the near-IR, extending the range of wavelength from ~ 1000 to 10^7 \AA . The model also carefully considers hydrogen collision and electron collision processes from quantum atomic data, particularly implementing ion-pair production and mutual-neutralization processes from Barklem (2018). Extensive details on the build-up of the atom and the corresponding atomic data are presented in Ezzeddine et al. (2016) and Ezzeddine et al. (2020).

2.1.3. NLTE Radiative Transfer

We utilize the NLTE radiative transfer code MULTI2.3 to solve for statistical equilibrium populations and derive the theoretical NLTE EW for the Fe I and Fe II lines in our atom. The code utilizes the Approximate Lambda Iteration (ALI) (Rybicki & Hummer 1991) to iteratively determine the populations using the comprehensive Fe I/Fe II model atom described in Section 2.1.2. MULTI2.3 also solves for LTE populations using the classical Saha and Boltzmann equations, which is output as a departure coefficient, b_i , where $b_i = n_i(\text{NLTE})/n_i(\text{LTE})$ (Wijbenga & Zwaan 1972), where n is the level population for the corresponding line transition i .

2.1.4. Linelist Selection

The linelist selection is crucial for the accurate derivation of Fe I and Fe II chemical abundances and stellar parameters using the EW

method, especially for cooler stars (e.g. FGK stars) since they have much denser spectral line regions containing blended lines. Therefore, we choose a comprehensive list of Fe I and Fe II from the *Gaia*-ESO line list (Jofré et al. 2014; Heiter et al. 2015, 2021), covering the wavelength ranges from 4750 to 6850 \AA and from 8500 to 8950 \AA . Additional lines from the R-Process Alliance (RPA) survey (e.g., Hansen et al. 2018; Sakari et al. 2018; Ezzeddine et al. 2020; Holmbeck et al. 2020) have also been added to account for lines common in metal-poor stars, with corresponding atomic data and references in (Roederer et al. 2018). We combine iron lines from both linelists, removing any duplicates in the process. Our final linelist is presented in Table 2.

2.2. Key Modules

Below we describe in detail the key components and modules of the LOTUS functionalities. An illustrated flow diagram of the workings of the code is also shown in Figure 1, demonstrating the connection between the different modules.

2.2.1. EW Interpolation Module

Traditional curve of growth (COG) methods to derive abundances do not take into account the inter-dependencies of the EW of the lines on stellar parameters such as T_{eff} , $\log g$, $[\text{Fe}/\text{H}]$ and v_{mic} . For some lines, however, EW can have strong and arbitrary dependencies on some atmospheric stellar parameters in given parameter space. Figure 2 and Figure 3 demonstrate these dependencies, where theoretical values for EW from our NLTE grid are shown as a function of T_{eff} and $\log g$ (left panel) and for T_{eff} and v_{mic} (right panel) for the Fe I line at 4070.768 \AA , and the Fe II lines at 6247.545 \AA , respectively. The metallicity for both plots has been fixed at $[\text{Fe}/\text{H}] = -2.00$ for demonstration purposes. It is clear that the EWs vary arbitrarily in the $T_{\text{eff}}\text{-}\log g$ space with resonance peaks show-

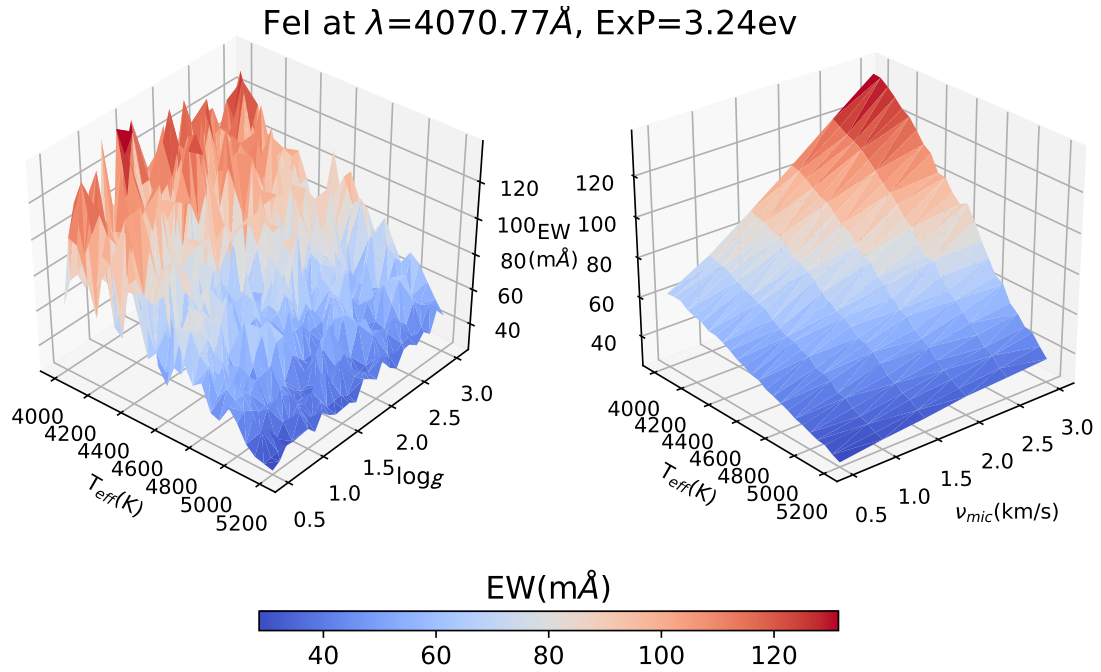


Figure 2. GCOG of EWs as a function of two-dimensional stellar parameters of the Fe I line at 4070.77\AA , with EP=3.24 eV. [Fe/H] is kept constant at -2.00 for demonstration purposes and to avoid cluttering the plot.

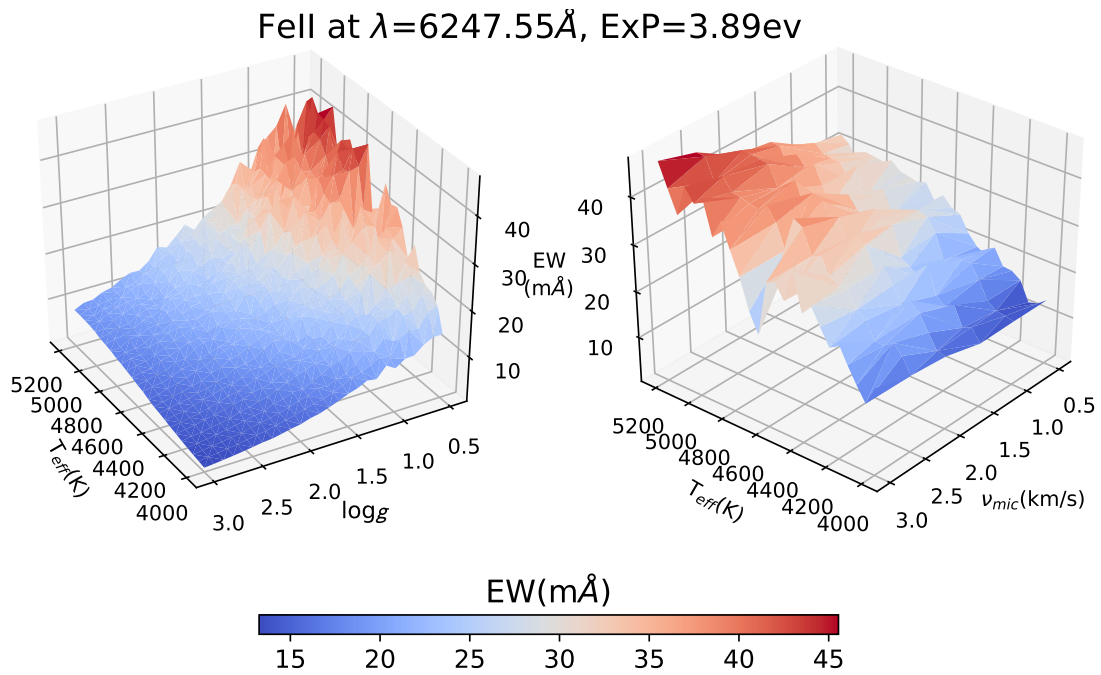


Figure 3. Same as Figure 2 but for the Fe II line at 6247.55\AA with EP=3.89 eV.

ing throughout the grid at different parameters while demonstrating a smoother dependence in the $T_{\text{eff}}-v_{\text{mic}}$ parameter space for the Fe I line at 4070 Å. The Fe II line at 6247 Å, however, shows smoother dependence on T_{eff} and $\log g$ for lower T_{eff} and higher $\log g$ values, with stronger resonance peaks showing at higher T_{eff} and lower $\log g$. We also observed this behavior when fixing Fe I abundances, in that increasing T_{eff} will decrease EW while EW is mostly insensitive to $\log g$ variation; For Fe II increasing T_{eff} will increase EW while increasing $\log g$ will decrease EW, which has been qualitatively proven in Chapter 17.5 of Hubeny & Mihalas (2014). To take into account such important dependencies in our codes, which can strongly affect our derived abundances and thus our stellar parameter derivation, we compute a Generalized Curve of Growth (GCOG) for each Fe I and Fe II line in our linelist. This takes into account each line's dependence on each of the stellar parameters, including T_{eff} , $\log g$, $[\text{Fe}/\text{H}]$, and v_{mic} . Such methods have also been implemented in previous work such as in Osorio et al. (2015) and Boeche & Grebel (2016). Interpolated GCOGs are then stored as libraries in our code, and utilized in the optimization module afterward to derive the Fe I and Fe II abundances.

2.3. Abundance Determination module

To derive the Fe I and Fe II abundances, we fit multivariate polynomials to each line, by deriving the relation between the iron abundance of the line with T_{eff} , $\log g$, v_{mic} and EW, denoted as $A(\text{Fe}) = P(T_{\text{eff}}, \log g, v_{\text{mic}}, \text{EW})$. The detailed form of P can be written as:

$$\sum_{i_1+i_2+i_3+i_4 \leq n} a_{i_1 i_2 i_3 i_4} (T_{\text{eff}})^{i_1} (\log g)^{i_2} (v_{\text{mic}})^{i_3} (\text{EW})^{i_4} \quad (1)$$

where i_m ($m=1,2,3,4$) is the power of the 3 stellar parameters (T_{eff} , $\log g$ and v_{mic}) as well as EW. Possible values for i_m are any positive integer as long as the sum of all these powers is

Table 1. Interpolation intervals chosen for different stellar types considered in LOTUS.

stellar parameter	types	intervals
T_{eff} (K)	K	[4000, 5200]
	G	[5200, 6000]
	F	[6000, 6850]
$\log g$	supergiant	[0.0, 0.5]
	giant	[0.5, 3.0]
	subgiant	[3.0, 4.0]
	dwarf	[4.0, 5.0]
$[\text{Fe}/\text{H}]$	very metal poor	[-3.5, -2.0]
	metal poor	[-2.0, -0.5]
	metal rich	[-0.5, 0.5]

less than or equal to the power degree of the polynomial n . $a_{i_1 i_2 i_3 i_4}$ is the product of the coefficients of each of these variables. The criteria for choosing n depends on the behavior of theoretical models within a specific parameter range of stellar parameters and is described in more detail in Section 2.3.1 below.

2.3.1. Selection of Interpolator

The selection of the linelist utilized to derive stellar parameters is dependent on the spectral type of the star, as some lines can be blended or strong in some cool high metallicity stars, whereas these same lines could also be blend-free and weaker for hotter, metal-poor stars. Therefore, the multivariate polynomial functions defined in Section 2.3 and used to derive the abundances of Fe I and Fe II lines depend on the choice of linelist. We thus pay special attention to the choice of interpolator by identifying the best selection of linelist per spectral type (or stellar parameters). Therefore, instead of interpolating in the whole parameter space for all the lines, we pre-define that the GCOGs fit only the abundances of the lines we pre-selected and chose to use within tested intervals of stellar parameters, according to an initial guess of spectral types that the users can insert as an

input in the code. Our choice of the intervals of different stellar parameters for each spectral types are listed in Table 1. For example, if an initial guess is chosen such that the target star is a metal-poor G giant, the multivariate polynomial will fit the abundance of each line versus other atmospheric parameters using the grid points falling into the range of T_{eff} from 5200 K to 6000 K, $\log g$ from 0.0 to 3.0 and $[\text{Fe}/\text{H}]$ from -2.0 to -0.5 .

In order to choose the best interpolator per spectral type (i.e., the optimal n) among several multivariate polynomials as defined in Equation 1, we use a Bayesian Information Criteria (BIC) to select the best polynomial function for each line based on the mean residual differences between the theoretical EWs at the nodes of our pre-computed NLTE grid (computed at a combination of T_{eff} , $\log g$, $[\text{Fe}/\text{H}]$, and v_{mic}), to the EWs interpolated at these parameters. We assume that the optimal model is among the polynomials with degree=2,3,4,5. The BIC was calculated such as:

$$\text{BIC} = n \ln \left(\frac{\text{SSR}}{n} \right) + k \ln(n) \quad (2)$$

where SSR is the sum of the squared residuals between the theoretical EWs and the interpolated EWs from models at specific nodes of the grid, and n is sample size (here we choose $n = 4000$ nodes in each spectral type interval). k is a free parameter (including coefficients and slope intercept), which can be calculated as $k=C_{d+4}^d$, where d is the degree of the polynomial, and 4 is chosen as the number of dependent variables for each interpolated EW (namely, T_{eff} , $\log g$, $[\text{Fe}/\text{H}]$ and v_{mic}).

We thus chose the best interpolator for each spectral type interval as that with the lowest BIC value. In Fig. 4, we show the differences between the interpolated EW using the lowest BIC interpolator as compared to the (non-interpolated) EW directly from MULTI2.3, categorized as a function of stellar spectral types

(x-axis) and metallicities (different panels). We observe that there exist no clear dependencies between differences and spectral types and metallicities. The average of differences is within 0.01 for all stellar spectral types and metallicities. We pre-define the default interpolated EW uncertainty (also a threshold for the lowest acceptable BIC) in LOTUS as $6 \text{ m}\text{\AA}$ for each line. However, we also design the code to allow users to input their acceptable uncertainty limits, in which case LOTUS will drop a given Fe I or Fe II from the linelist if the computed BIC is larger than this uncertainty, and will subsequently be excluded from the lines used to derive the stellar parameters in the optimization module.

2.3.2. EP Cut-off

The NLTE abundances derived from low excitation potential Fe I can yield larger abundances as compared with those derived from high-excitation Fe I and Fe II lines, especially using 1D atmospheric models (Amarsi et al. 2016). Such differences can reach up to 0.45 dex for some Fe I lines, and can affect our derived stellar parameters as documented in several studies including Bergemann et al. (2012); Lind et al. (2012) as well as others. We thus follow previous literature studies by introducing low-excitation potential cut-offs for Fe I lines with $\text{EP}(\text{Fe I}) < 2.7\text{eV}/2.5\text{eV}/2.0\text{eV}$ for stars with $[\text{Fe}/\text{H}] < -0.5$, depending on the number of Fe I and Fe II lines measured in the stars and the optimization convergence criteria (see Section 2.4); We conduct no cut-offs for stars with $[\text{Fe}/\text{H}] > -0.5$.

2.4. Optimization Module

Once reliable linelists and interpolators per spectral types of input target stars have been chosen, as explained in Section 2.3 above, the derived Fe I and Fe II abundances are fed into the optimization module with an initial guess of the general type of the target star. We note that users don't need to specify an initial guess

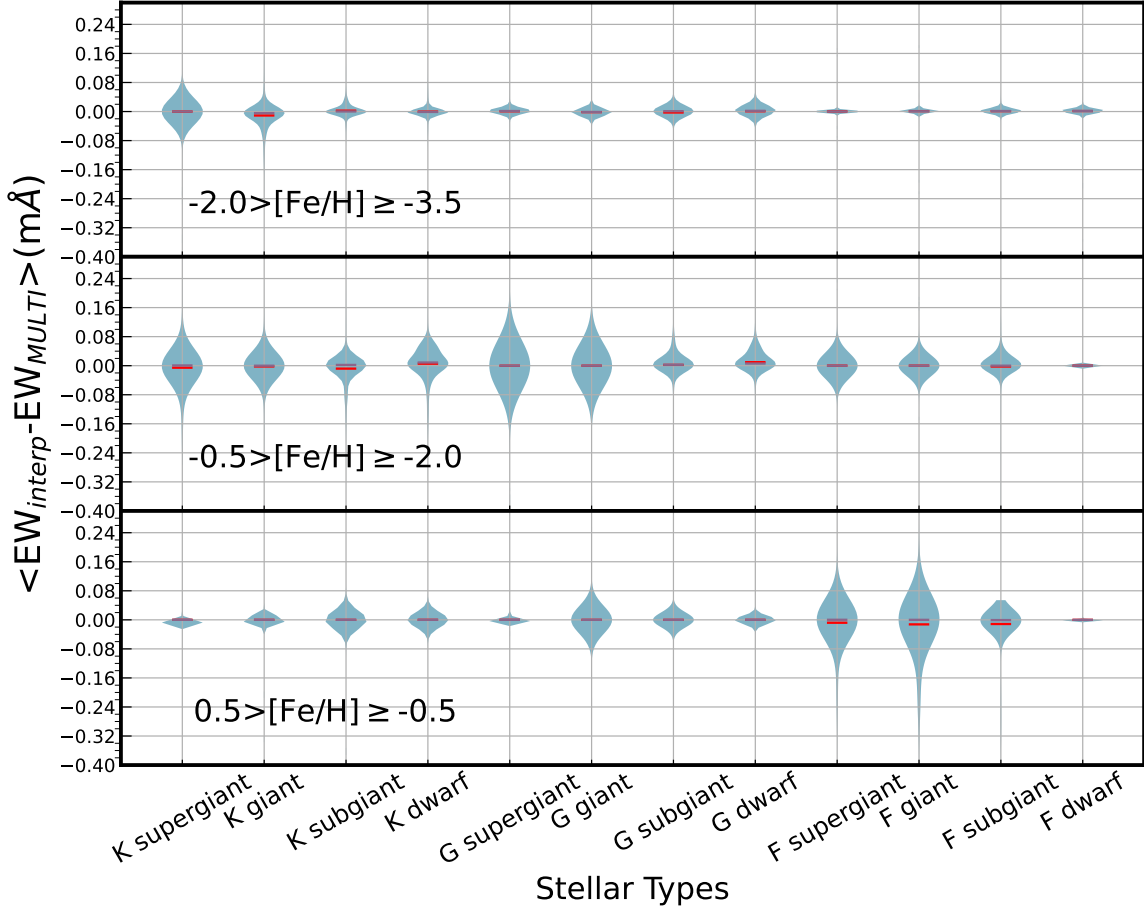


Figure 4. Differences (in mÅ) between the interpolated EWs (using interpolators chosen at the lowest BIC values) and the EWs from NLTE theoretical calculations computed directly using MULTI2.3. Each violin plot shows the distribution of the means of such differences for a random 4000 nodes within the spectral type interval of the pre-computed EW library. Red lines are marked as the means of the distributions while purple lines are for the medians. The differences are shown for different metallicity ranges as indicated in each panel.

of each stellar parameter, as it suffices to only chose an initial guess of the spectral type as an input to LOTUS, which is then assigned the corresponding interpolation parameters interval as indicated in Table 1.

2.4.1. Optimization Conditions

The general principle of optimization is to adjust stellar parameters iteratively to derive optimal combinations of stellar parameters that can satisfy the following three conditions: (i) excitation equilibrium, or minimizing the trend (i.e., slope) of the Fe I abundances as a function of excitation potential EP, (ii) ensuring ionization

equilibrium or minimizing the differences between the abundances derived from the Fe I and Fe II lines, and (iii) minimizing the trend (i.e., slope) between the abundances derived from the Fe I lines versus the reduced equivalent widths, $REW = \log(EW/\lambda)$.

Therefore, we derive T_{eff} by ensuring excitation equilibrium, $\log g$ by ensuring ionization equilibrium, and v_{mic} by minimizing the trend between Fe I abundances versus line strength (REW). $[\text{Fe}/\text{H}]$ was then determined by averaging the abundances derived from the Fe I and Fe II abundances.

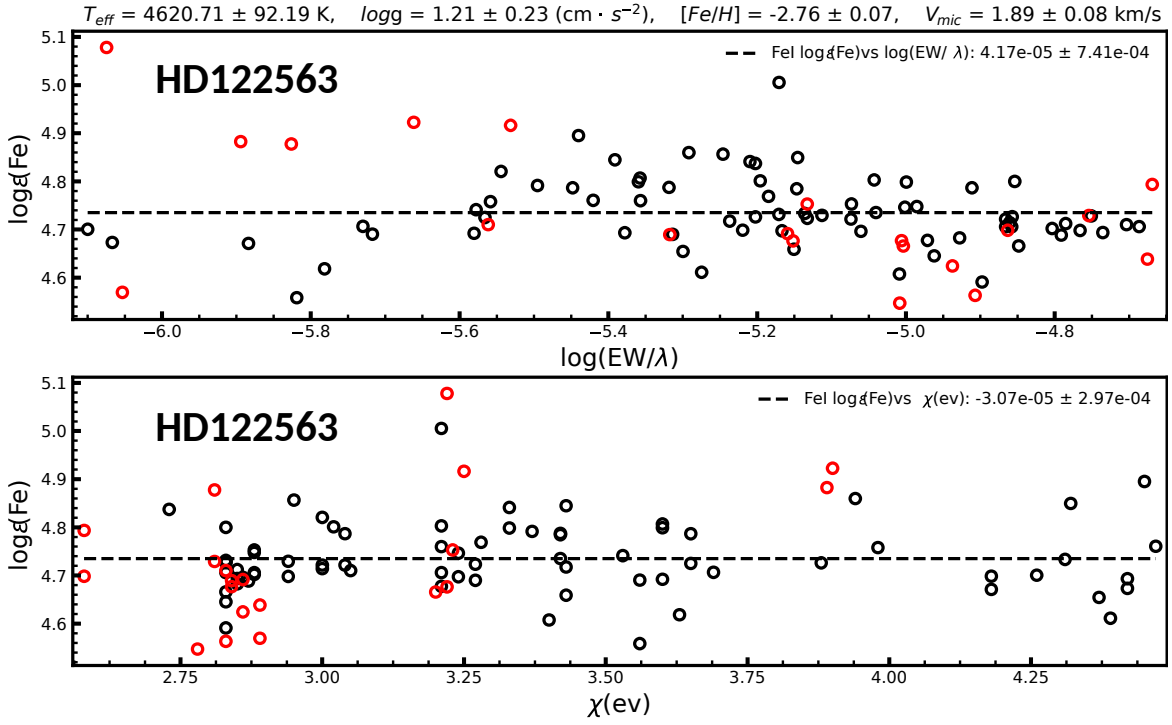


Figure 5. Derived Fe I (black circles) and Fe II (red circles) line abundances versus reduced equivalent widths (upper panel) and excitation potential energies χ (lower panel) for selected lines in the metal-poor benchmark star HD122563. The parameters indicated on the top are the optimal values derived using the global minimization (differential evolution) algorithm in LOTUS. Dotted lines are the best linear fits to the Fe I lines in each panel. The labels at the upper left corner of each panel are the slopes of the fits and their corresponding standard deviations.

2.4.2. Targeted Optimized Object Function

In order to find the best combination of stellar parameters that satisfy the optimization conditions defined in Section 2.4.1 within our parameter grid, we first combine these conditions into a targeted optimization object function \mathcal{F} , such as:

$$\mathcal{F} = \left(\frac{s_{\chi,1}}{\sigma_{\chi,1}} \right)^2 + \left(\frac{s_{REW,1}}{\sigma_{REW,1}} \right)^2 + \left(\frac{\bar{A}_1 - \bar{A}_2}{\sigma_{1-2}} \right)^2 \quad (3)$$

where the subscripts "1" and "2" correspond to Fe I and Fe II, respectively. $s_{\chi,1}$ is the slope between Fe I abundances and EP, and $\sigma_{\chi,1}$ is its uncertainty, $s_{REW,1}$ is the slope between the Fe I abundances and REW, and $\sigma_{REW,1}$ is its uncertainty. \bar{A}_1 and \bar{A}_2 are the mean abundances for Fe I and Fe II, respectively, while σ_{1-2} is the standard deviation of the differences between \bar{A}_1 and \bar{A}_2 . A converged solution is obtained at

the combination of T_{eff} , $\log g$, $[\text{Fe}/\text{H}]$ and v_{mic} , which minimizes \mathcal{F} globally.

2.4.3. Global minimization

To find the global minimization fit parameters within our grid, we adopt a differential evolution algorithm implementing a global minimization search. The goal is to minimize \mathcal{F} by starting with an initial population of candidate solutions, which are iteratively improved by retaining the fittest solutions that yield a lower \mathcal{F} values, until convergence for the best-fit parameters is met (Storn & Price 1996). The advantage of a differential evolution algorithm is that it has the benefit of handling nonlinear and non-differentiable multi-dimensional objective functions while requiring few control parameters to steer the minimization. For our code, we select 100 initial populations (sets of solutions) with a combined rate of 0.3, which is a crossover prob-

ability that depends on how fast the algorithm moves to the next generation of populations. We try different weights between 0.8 and 1.2, to maintain a proper searching radius, at the same time making sure it does not slow down the convergence speed. We adopt $\mathcal{F} \sim 10^{-5}$ as the absolute tolerance for each iteration. After each iteration, we perform a 3σ -clipping on the abundances of the Fe I and Fe II lines to remove outliers. We adopt 3 iterations of outlier removing in total as a default, however, this number can be defined by the users depending on the quality of their EW measurements. An example of HD122563 with derived abundances of Fe I and Fe II versus REW and EP at optimal atmospheric parameters is shown in Figure 5.

2.5. Uncertainty Estimation Module

Since \mathcal{F} is a function of the stellar parameters, it can be described as $\mathcal{F}(\theta) = \mathcal{F}(T_{\text{eff}}, \log g, v_{\text{mic}})$. We can keep track of how \mathcal{F} changes along the perturbations around the optimal solution $\theta^* = (T_{\text{eff}}^*, \log g^*, v_{\text{mic}}^*)$, T_{eff}^* , $\log g^*$ and v_{mic}^* are the parameters at the optimal solution. Indeed, \mathcal{F} resembles a likelihood function, which can be used to estimate the uncertainties on each of our derived stellar parameters from the Hessian Matrix such as:

$$SE(\theta^*) = \text{diag}(\sqrt{\mathcal{H}^{-1}(\theta^*)}) \quad (4)$$

where the Hessian Matrix for our objective function can be written as:

$$\mathcal{H}(\theta) = \frac{\partial}{\partial \theta_i \partial \theta_j} \mathcal{F}(\theta), 1 \leq i, j \leq 3 \quad (5)$$

For [Fe/H], we adopt the standard deviation of the Fe I lines as the uncertainty.

However, in the above uncertainty framework, one strong assumption is that the standard errors obtained are symmetric around the mean values. This is only true if the probability distribution function of the derived parameters is a normal distribution. Normally, this is not the

case. We, therefore, use a Bayesian framework to robustly determine the uncertainties on our derived stellar parameters. First, we construct a log-likelihood function using the same terms as in Equation 3 such as:

$$\log(\mathcal{L}) = -\frac{1}{2} \sum_{i \leq 3} \left[\left(\frac{s_i}{n_i} \right)^2 + \log(2\pi n_i) \right] \quad (6)$$

where n_i can be written as:

$$n_i = \sigma_i^2 + f^2 s_i^2 \quad (7)$$

where s_i represent the slopes $s_{\chi,1}$, $s_{REW,1}$ and $\bar{A}_1 - \bar{A}_2$ individually, while σ_i are their corresponding standard deviations. Introducing f will compensate the underestimation of the variance of each parameter assuming such an additional term is proportional to the model itself.

We then perform the Slice Sampling algorithm (Neal 2003), which is a type of Markov Chain Monte Carlo (MCMC) implemented in PyMC3, to complete the estimation of the posterior probability of each parameter. This method adjusts the step size automatically on every proposed candidate to match the profile of the posterior distribution without the need to choose a transition function. Such a framework ensures higher efficiency as compared to classical MCMC algorithms, such as Metropolis and Gibbs (Metropolis & Ulam 1949; Geman & Geman 1984). For all stellar parameters, we derive a normal distribution around the mean optimized value obtained from the global minimization module described in Section 2.4.3, and a standard deviation determined from the standard errors of the Hessian Matrix.

We use the logarithmic of f as an input variable to the MCMC sampler with a uniform distribution ranging from -10 to 1 . In the sampling process, we consider 4 running chains with each containing 1000 draw steps and 200 tunes steps. Figure 6 shows the output from our posterior distribution of the stellar parameters

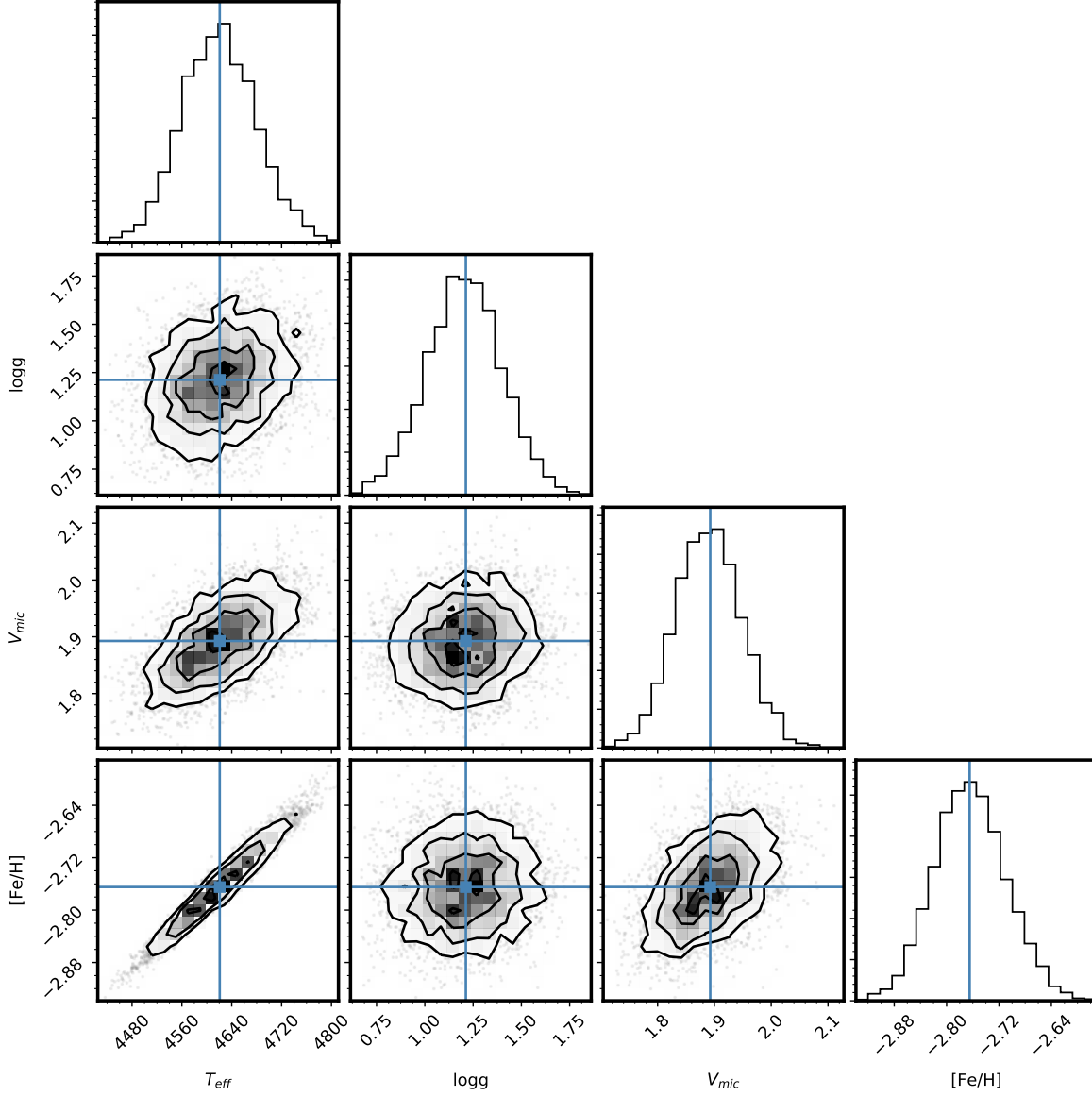


Figure 6. Marginalized posterior distributions of the stellar parameters of HD122563 based on the log-likelihood function in Equation 6. 1σ , 2σ and 3σ uncertainty region are denoted as solid contours in the two dimensional plot. The histograms show the marginalized posterior distributions for each parameter, respectively. Blue intersecting lines show the values obtained from our global optimization module.

and their uncertainty regions for a benchmark metal-poor star, HD122563. On the same plot, we also show the optimized parameters derived using our global optimization module (blue lines intersection), which agree very well.

3. TESTING LOTUS

We test LOTUS by deriving the atmospheric stellar parameters of benchmark stars with well constrained non-spectroscopic and fundamental

stellar parameters, to quantify the precision of our derived parameters and their uncertainties. Below we present the results of these tests. We list the derived stellar parameters (T_{eff} , $\log g$, $[\text{Fe}/\text{H}]$ and v_{mic}) using LOTUS in LTE and NLTE of all the stars considered from Section 3.1 to 3.4 below, the sources of the EW, the number of Fe I and Fe II lines, and the excitation potential cut-offs for each star in Table 3.

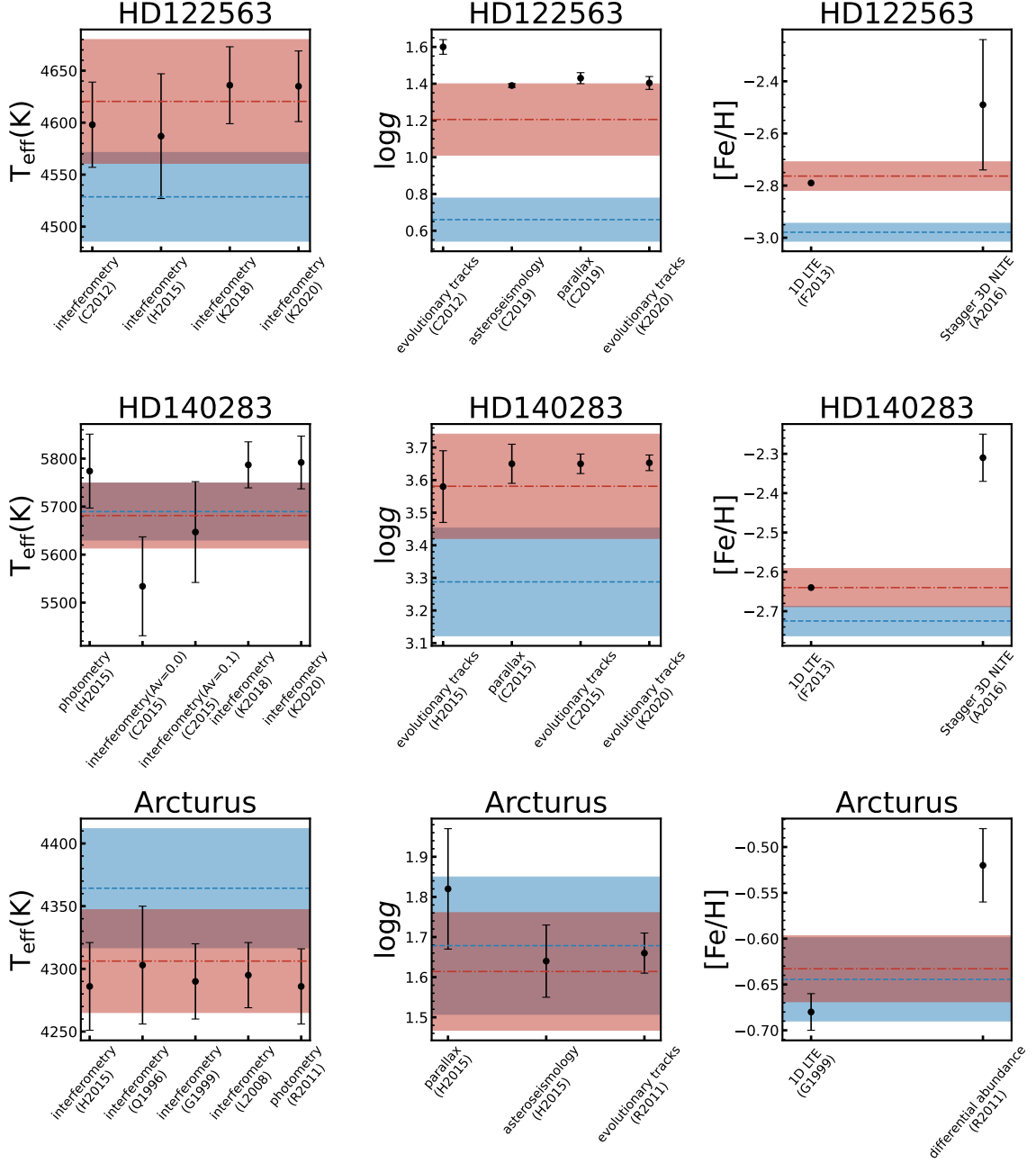


Figure 7. Comparison of our derived stellar parameters, T_{eff} , $\log g$ and $[\text{Fe}/\text{H}]$ using LOTUS to reference literature values derived non-spectroscopically (for T_{eff} and $\log g$) for HD122564, HD140283 and Arcturus. The mean NLTE values (red dashed lines) with their 1σ confidence intervals (red shadow areas) and our mean LTE values (blue dashed lines) with their 1σ confidence intervals (blue shadow areas), compared to reference stellar parameters (black dots with error bars) for references on the x-axis. References are as follows: Q1996...Quirrenbach et al. (1996); G1999...Griffin & Lynas-Gray (1999); L2008...Lacour et al. (2008); R2011...Ramírez & Allende Prieto (2011); C2012...Creevey et al. (2012); F2013...Frebel et al. (2013); H2015...Heiter et al. (2015); C2015...Creevey et al. (2015); A2016...Amarsi et al. (2016); K2018...Karovicova et al. (2018); C2019...Creevey et al. (2019); K2020...Karovicova et al. (2020).

3.1. HD122563, HD140283, and Arcturus

The two metal-poor standard stars HD122563, HD140283 and the benchmark gi-

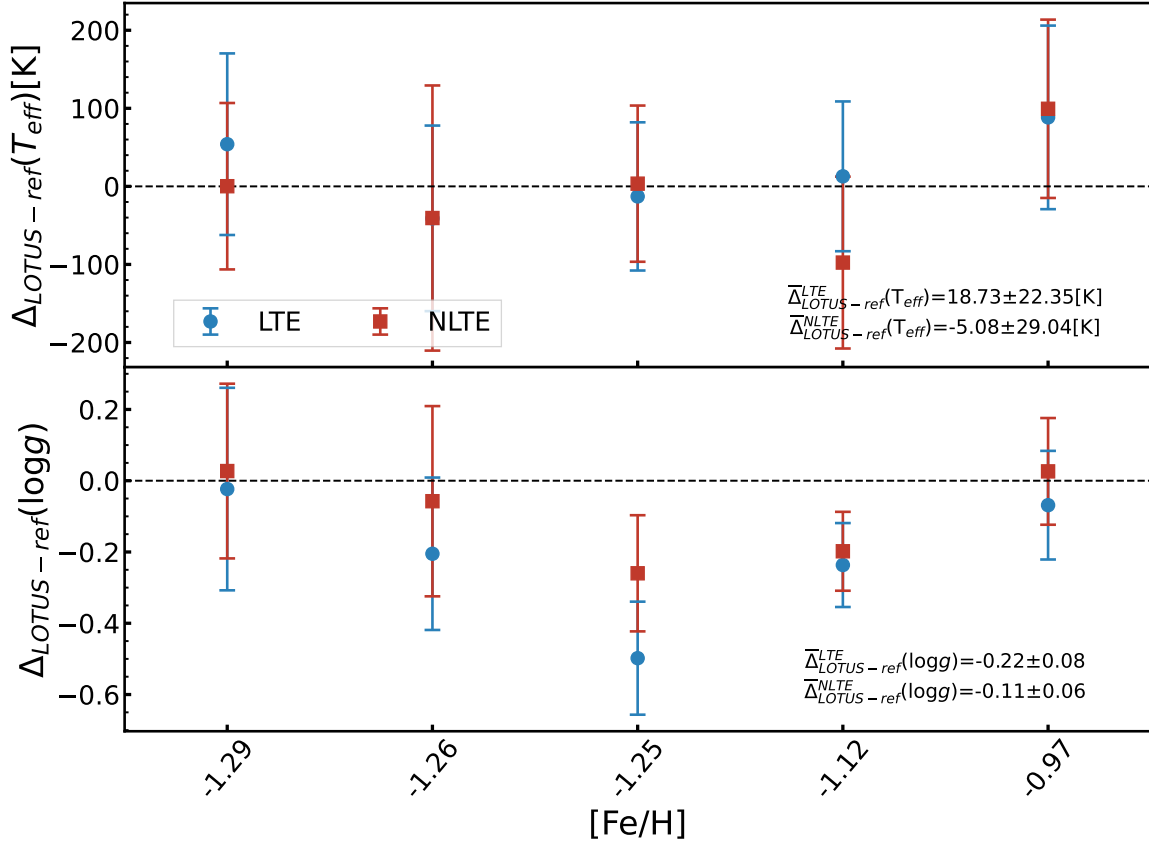


Figure 8. Differences in $\log g$ and T_{eff} between values derived using LOTUS versus reference values from Hawkins et al. (2016) for five GES metal-poor stars in their sample. Blue circles are LTE differences, while red squares are NLTE. Dashed lines in both panels are the zero baselines. Average systematic offsets are included in the text of each panel.

ant Arcturus have been widely analyzed independently in the literature. Their stellar parameters have therefore been derived spectroscopically (using 1D, 3D, LTE and NLTE assumptions, or a combination of each), as well as using non-spectroscopic methods and fundamental equations (e.g., using photometric calibrations, asteroseismology, or interferometric angular diameters). All three stars are dubbed benchmark stars which have been selected as comparison standards for the largest stellar surveys, especially in the *Gaia*-ESO spectroscopic survey (Jofré et al. 2014; Heiter et al. 2015). We adopt EW measurements of each benchmark star from literature publications as follows: HD122563 (Frebel et al. 2013), HD140283 (Frebel et al. 2013), Arcturus (Jofré

et al. 2014). Frebel et al. (2013) measured their EW from high-resolution spectroscopic observations ($R \sim 35,000$ in the blue and $\sim 28,000$ in the red) of HD122563 and HD140283, obtained with the MIKE spectrograph (Bernstein et al. 2003) on the Magellan-Clay telescope at Las Campanas. A $R \geq 70,000$ spectrum was used to derive EW for Arcturus from the VLT spectrum (Jofré et al. 2014). We derive the stellar parameters of each star and their uncertainties using LOTUS. We then compare our NLTE and LTE parameters with several independent determinations from the literature, as shown in Figure 7.

$$\begin{array}{l} \text{HD122563—We} \\ \log g = 1.21 \pm 0.19, \end{array} \quad \begin{array}{l} \text{derive} \\ T_{\text{eff}} = 4620 \pm 59 \text{ K}, \\ v_{\text{mic}} = 1.89 \pm 0.06 \text{ km s}^{-1} \end{array}$$

and $[\text{Fe}/\text{H}] = -2.76 \pm 0.05$ in NLTE, and $T_{\text{eff}} = 4528 \pm 42 \text{ K}$, $\log g = 0.66 \pm 0.12$, $v_{\text{mic}} = 1.84 \pm 0.03 \text{ km s}^{-1}$ and $[\text{Fe}/\text{H}] = -2.98 \pm 0.03$. Creevey et al. (2012) derived $T_{\text{eff}} = 4598 \pm 41 \text{ K}$ using an angular diameter observed with CHARA interferometry and Palomar interferometric observations. Heiter et al. (2015) derived $T_{\text{eff}} = 4587 \pm 60 \text{ K}$ based on the angular diameters and bolometric flux calibrations, and $\log g = 1.44 \pm 0.24$ from fitting evolutionary tracks. Karovicova et al. (2018) updated CHARA interferometry with more data and derived an effective temperature of $T_{\text{eff}} = 4636 \pm 37 \text{ K}$. Later in Karovicova et al. (2020), they updated their data reduction pipeline and derived a new $T_{\text{eff}} = 4635 \pm 34 \text{ K}$. Our NLTE T_{eff} derived for HD122563 agrees very well with T_{eff} determined in these studies using interferometric angular diameters, within $\sim 30 \text{ K}$, while the LTE T_{eff} deviated by $\sim 100 \text{ K}$ from the reference values.

And for $\log g$ results from the recent updated asteroseismic analysis are in agreement with the NLTE values in our work, which is close to the upper limit of 1σ confidence interval.

For $\log g$, Creevey et al. (2012) used evolutionary track models to derive $\log g = 1.60 \pm 0.04$ for HD122563, while Creevey et al. (2019) utilized the Hertzsprung telescope (SONG network node) to accurately measure the surface gravity of HD122563 using asteroseismology for the first time, and derived $\log g = 1.39 \pm 0.01$. In their paper they also compare to *Gaia* DR2 parallax-based $\log g = 1.43 \pm 0.03$, which shows high consistency between these methods. Karovicova et al. (2020) also used evolutionary track models to derive $\log g = 1.404 \pm 0.03$ for the same star. Our LOTUS $\log g = 1.22$ in NLTE matches within ~ 0.1 dex the asteroseismic and parallax $\log g$ in Creevey et al. (2019), whereas the LTE value is 0.6 dex lower. This gives us strong confidence in LOTUS' ability to derive NLTE surface gravities from spectroscopic observations.

We then compare our NLTE and LTE $[\text{Fe}/\text{H}]$ with those derived by Frebel et al. (2013) in 1D, LTE and Amarsi et al. (2016) in 3D,NLTE. Our NLTE $[\text{Fe}/\text{H}]$ agrees with that determined in both studies within error bars, although Amarsi et al. (2016) derived a higher $[\text{Fe}/\text{H}] = -2.5$, which is likely due to considering 3D effects in their study.

HD140283—We derive $T_{\text{eff}} = 5681 \pm 67 \text{ K}$, $\log g = 3.58 \pm 0.16$, $v_{\text{mic}} = 2.17 \pm 0.16 \text{ km s}^{-1}$ and $[\text{Fe}/\text{H}] = -2.64 \pm 0.05$ in NLTE, and $T_{\text{eff}} = 5689 \pm 59 \text{ K}$, $\log g = 3.29 \pm 0.17$, $v_{\text{mic}} = 2.09 \pm 0.14 \text{ km s}^{-1}$ and $[\text{Fe}/\text{H}] = -2.72 \pm 0.04$ in LTE. Heiter et al. (2015) derived a mean $T_{\text{eff}} = 5774 \pm 77 \text{ K}$ for the sub-giant in their *Gaia*-ESO benchmark sample from photometric calibrations. Additionally, Creevey et al. (2015) used the VEGA interferometer on CHARA to determine $T_{\text{eff}} = 5534 \pm 103 \text{ K}$ (using $A_V = 0.0$ mag) and $T_{\text{eff}} = 5647 \pm 105 \text{ K}$ (using $A_V = 0.1$ mag). Karovicova et al. (2018) similarly derived an updated $T_{\text{eff}} = 5787 \pm 48 \text{ K}$ from additional interferometric data points, and afterwards updating their values to $5792 \pm 55 \text{ K}$ in Karovicova et al. (2020). Our LTE and NLTE T_{eff} for HD140283 agree with the interferometric values derived in Creevey et al. (2015) within 120 K and Karovicova et al. (2018, 2020) within 80 K.

Heiter et al. (2015) derived $\log g = 3.58 \pm 0.11$ using fundamental relations and adopting independently derived parallax for the star. Creevey et al. (2015) also derived a mean $\log g = 3.69 \pm 0.03$, similarly from a combination of parallax and evolutionary track models. Both $\log g$ determined by parallax methods in Heiter et al. (2015) and Creevey et al. (2015) agree well with our NLTE value to within 0.05 dex. Karovicova et al. (2020) derived $\log g = 3.65 \pm 0.0$ from evolutionary models. Our LTE values is, unexpectedly, 0.3 dex lower.

Similar to HD122563, we compare our $[\text{Fe}/\text{H}]$ with 1D,LTE and 3D,NLTE abundances in

Frebel et al. (2013) and Amarsi et al. (2016), respectively. Given that both studies derived their abundances by fixing T_{eff} and $\log g$, while ours were derived simultaneously using the global optimization method adopted in LOTUS, we warrant serious direct comparison with their values. Nevertheless, our NLTE values agree very well with that derived in Frebel et al. (2013) within 1σ , whereas is 0.3 dex lower as compared to Amarsi et al. (2016).

Arcturus—We derive $T_{\text{eff}} = 4306 \pm 41$ K, $\log g = 1.61 \pm 0.15$, $v_{\text{mic}} = 1.79 \pm 0.02$ km s⁻¹ and $[\text{Fe}/\text{H}] = -0.63 \pm 0.04$ in NLTE, and $T_{\text{eff}} = 4364 \pm 47$ K, $\log g = 1.68 \pm 0.17$, $v_{\text{mic}} = 1.76 \pm 0.02$ km s⁻¹ and $[\text{Fe}/\text{H}] = -0.64 \pm 0.05$ in LTE. For T_{eff} Quirrenbach et al. (1996) used the MkIII Optical Interferometer on Mt. Wilson to determine Arcturus’ angular diameter and derived $T_{\text{eff}} = 4303 \pm 47$ K. Griffin & Lynas-Gray (1999) collected all literature results of interferometry observation up to their study and derived $T_{\text{eff}} = 4290 \pm 30$ K. Lacour et al. (2008) used the IOTA 3 telescope interferometer in the H band to derive $T_{\text{eff}} = 4295 \pm 26$ K. Additionally, Ramírez & Allende Prieto (2011) fit theoretical spectral energy distributions (SED) from visible blue bands to mid-infrared to derive $T_{\text{eff}} = 4286 \pm 30$ K. Finally, Heiter et al. (2015) derived a mean of 4274 ± 83 K from different interferometric measurements, even though they warranted against using Arcturus as a benchmark given the large dispersion they obtained. All interferometric T_{eff} agree very well with our NLTE T_{eff} to within ~ 20 K. Our LTE value is, however, ~ 80 K higher.

Ramírez & Allende Prieto (2011) derived $\log g = 1.66 \pm 0.05$ from HIPPARCOS parallax and isochrone fitting, while Heiter et al. (2015) derived a fundamental $\log g = 1.64 \pm 0.09$ based on seismic mass and $\log g = 1.82 \pm 0.15$ from a compilation of parallax-based measurements. Our NLTE $\log g$ agrees very well with both results, whereas our LTE values is 0.1 dex higher.

Griffin & Lynas-Gray (1999) derived $[\text{Fe}/\text{H}] = -0.68 \pm 0.02$ by comparing theoretical 1D, LTE SEDs with observed flux. Ramírez & Allende Prieto (2011) used a differential abundance analysis relative to the solar spectrum to derive $[\text{Fe}/\text{H}] = -0.52 \pm 0.04$. Our NLTE and LTE $[\text{Fe}/\text{H}]$ are within 0.05 dex from each other, and agree well with the values derived in Griffin & Lynas-Gray (1999) while being ~ 0.1 dex as compared to differential abundance analysis in Ramírez & Allende Prieto (2011).

3.2. GES Metal-Poor Stars

We also test LOTUS on five metal-poor benchmark stars proposed by Hawkins et al. (2016) from the *Gaia*-ESO survey (GES). They determined T_{eff} via the Infrared Flux Method (IRFM) (Casagrande et al. 2011) using multi-band photometry and $\log g$ by fitting to evolutionary stellar models. The Fe I and Fe II EWs for the sample stars were adopted from Hawkins et al. (2016), who used different EW measurements from different pipelines from the GES survey to derive their parameters. We use their EPINARBO (EPI) EWs derived with the FAMA pipeline following Magrini et al. (2013), as those were derived consistently. We compare our derived T_{eff} and $\log g$ using LOTUS to those in Hawkins et al. (2016) using the same Fe I and Fe II lines. We find that our NLTE parameters are on average within 5 ± 29 K from their T_{eff} and 0.11 ± 0.06 for $\log g$ on average, whereas our LTE parameters are within 18 ± 22 K and 0.22 ± 0.08 dex for T_{eff} and $\log g$ respectively. Star by star comparisons are shown in Figure 8. Our NLTE parameters agree better with the non-spectroscopic parameters from Hawkins et al. (2016), as compared to LTE.

A larger $\log g$ dispersion is obtained for HD106038 though with $[\text{Fe}/\text{H}] = -1.25$ of -0.25 and -0.45 , for both our NLTE and LTE results, respectively. With a 3D, Non-LTE analysis, and *Gaia* EDR3 parallax, Giribaldi et al. (2021) derived $\log g = 4.29 \pm 0.04$, which is in ex-

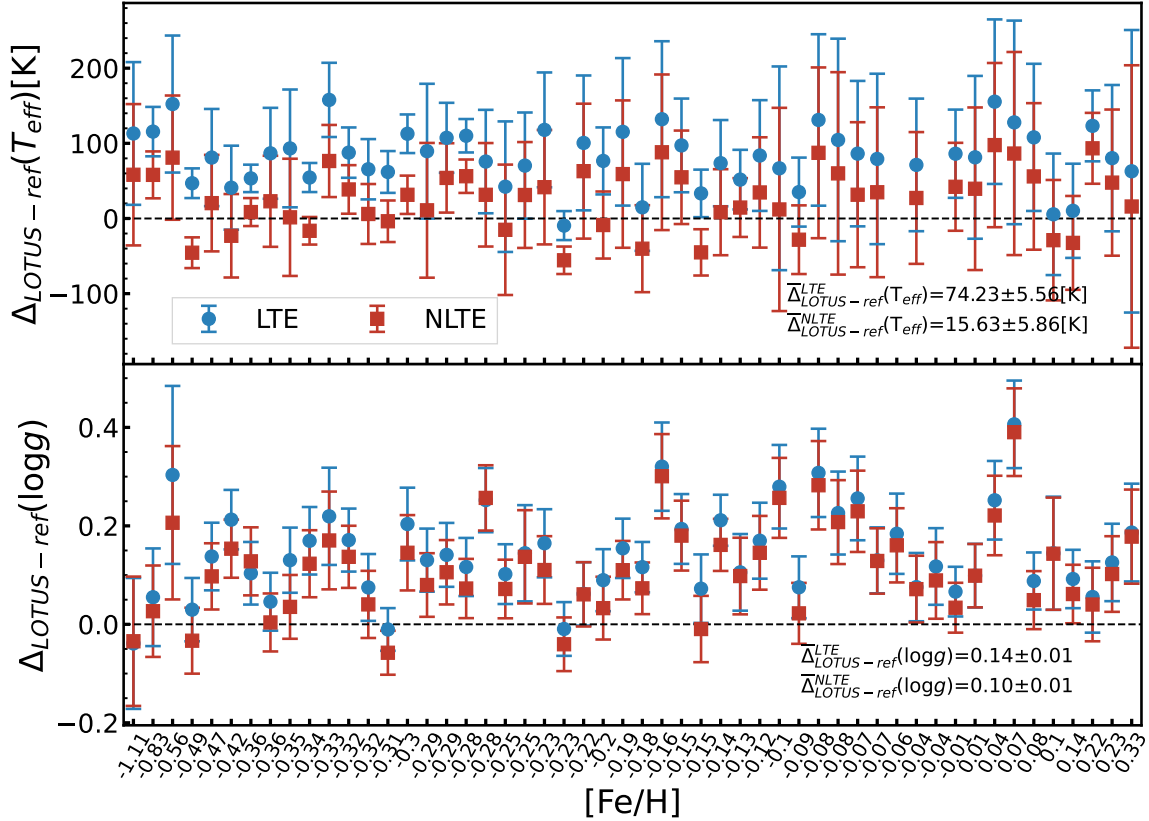


Figure 9. Same as in Figure 8 for the GES-K2 sample stars from [Worley et al. \(2020\)](#).

cellent with our NLTE $\log g = 4.29 \pm 0.08$. Additionally, only 35 Fe I lines used by [Hawkins et al. \(2016\)](#) were used to derive the stellar parameters in LOTUS which decreases the accuracy of optimal values (see Section 5 for more details).

3.3. GES-K2 Stars

We also test LOTUS by deriving atmospheric stellar parameters of a sample of Kepler-2 (K2) star sample, which was also observed using a high-resolution UVES spectrograph on the VLT as part of the GES survey. [Worley et al. \(2020\)](#) combined the high-resolution spectroscopic observations from UVES, photometry, and precise asteroseismic data from K2 to derive self-consistent stellar parameters for these stars, which represent a good non-spectroscopic sample to compare our stellar parameters derived with LOTUS to.

We adopt the EW measurements from [Worley et al. \(2020\)](#) derived from high-resolution

UVES spectroscopic observations. We chose a total of 52 stars from their sample. The majority of the stars in the sample are metal-rich with $[\text{Fe}/\text{H}] > -0.5$. Only six stars have $[\text{Fe}/\text{H}] < -0.5$. [Worley et al. \(2020\)](#) used the IRFM to determine photometrically calibrated T_{eff} for all their stars following [Casagrande et al. \(2010, 2011\)](#).

The average uncertainties reported in [Worley et al. \(2020\)](#) for T_{eff} and $\log g$ of the GES-K2 stars are ± 65 K and ± 0.02 , respectively. We note that these values are close to our parameter grid resolution. We derive the stellar parameters for the 52 GES-K2 stars using LOTUS. Our results for $\log g$ and T_{eff} as compared to [Worley et al. \(2020\)](#) are shown in Figure 9 as a function of $[\text{Fe}/\text{H}]$. We find that the average differences between the LOTUS parameters are $\bar{\Delta}T_{\text{eff}} = 74 \pm 6$ K and $\bar{\Delta}\log g = 0.14 \pm 0.01$ in LTE, and $\bar{\Delta}T_{\text{eff}} = 16 \pm 6$ K, $\bar{\Delta}\log g = 0.10 \pm 0.01$ in NLTE. Both LTE and NLTE parameters

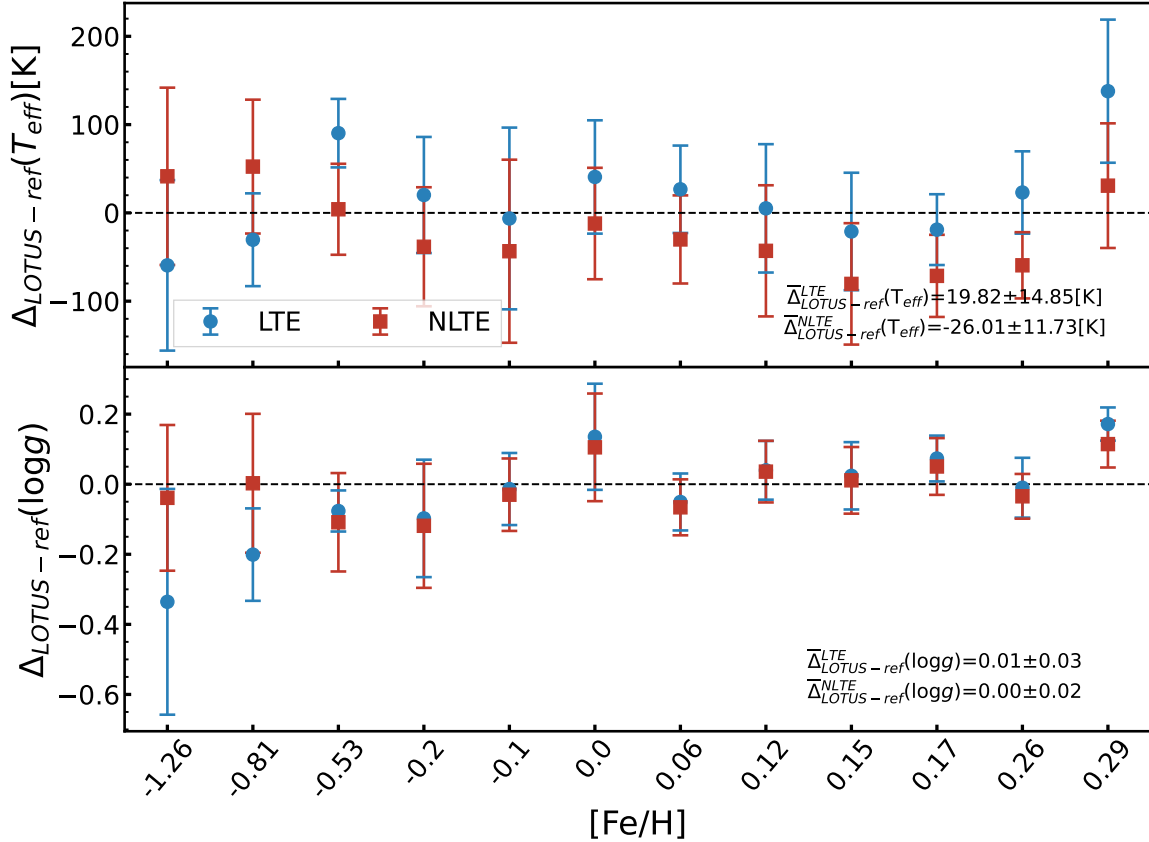


Figure 10. Same as in Figure 8 for the CHARA sample stars from Karovicova et al. (2020, 2021a,b).

agree well with the photometric and asteroseismic parameters from Worley et al. (2020) within their error bars, however our NLTE parameter derivations agree better for both T_{eff} and, particularly for $\log g$.

3.4. CHARA Interferometry Stars

Finally, we apply and test LOTUS on a sample of stars with effective temperatures derived homogeneously from interferometric angular diameters observed by CHARA from Karovicova et al. (2020, 2021a,b). Karovicova et al. (2020) presented a study of interferometric observations of ten late-type metal-poor dwarfs and giants, whereas Karovicova et al. (2021a,b) showed a similar analysis for several metal-rich stars. For three of their stars (namely, HD122563, HD140283, and HD175305), we have already presented their analysis in Section 3.1 and 3.2. We, therefore, do not include

the analysis of these stars again in this section. EW measurements of the total 12 stars were adopted from different literature sources including Takeda et al. (2005); Morel et al. (2014); Heiter et al. (2015); Takeda & Tajitsu (2015); Liu et al. (2020). The average uncertainties of the interferometric T_{eff} estimated by Karovicova et al. (2020, 2021a,b) are within 1%. The authors derived their $\log g$ values by fitting Dartmouth isochrones (Dotter et al. 2008) to their interferometric T_{eff} . They thus derive median uncertainties for $\log g$ of 0.09 for their metal-poor star sample, 0.05 for their dwarf sample, and 0.07 for the giants/subgiants sample.

We find that on average the differences in T_{eff} and $\log g$ between the reference values (Karovicova et al. 2020, 2021a,b) and those derived with LOTUS are within 26 K and 0.01 in NLTE, respectively. The NLTE parameters derived for all the stars agree within 1σ as compared to

the reference values, except for the $\log g$ value of HD121370 with $[\text{Fe}/\text{H}]=0.29$, which deviated by 0.12 for LTE and 0.18 for NLTE. Heiter et al. (2015), however, reported a seismic $\log g$ for this star of 3.83 ± 0.02 dex, which agrees very well with our NLTE result of 3.91 ± 0.06 within 1σ .

4. NLTE CORRECTIONS

The stars presented in Section 3 for testing LOTUS on benchmark stars with T_{eff} and $\log g$ derived using non-spectroscopic methods cover a limited range of metallicities (mostly with $[\text{Fe}/\text{H}] > -1.0$), as well as mainly dwarfs and sub-giant stars. However, NLTE stellar parameter “corrections” (also known as NLTE effects, defined as $\Delta \text{NLTE} = \text{parameter}(\text{NLTE}) - \text{parameter}(\text{LTE})$) have been shown in the literature to be more significant and important for evolved (giants and supergiant) metal-poor stars Lind et al. (2012); Ezzeddine et al. (2017). Thus, to be able to test our derived NLTE “corrections” on a larger, more metal-poor sample of giant stars, we derive LTE and NLTE stellar parameters for the *R*-process Alliance giant metal-poor star sample from Hansen et al. (2018), who derived the stellar parameters of 107 metal-poor stars ($[\text{Fe}/\text{H}] < -1.0$) selected based on their *r*-process enhancement from several surveys. The EW measurements for Fe I and Fe II lines were adopted from Hansen et al. (2018), measured from their du Pont spectroscopic observations. We thus add the RPA sample stars to our test sample stars presented in Section 3, resulting in a significant sample covering a wide representative range of stellar parameters from $T_{\text{eff}}=4000$ to 6500 K, $\log g=0.0$ to 4.5, and $[\text{Fe}/\text{H}]=-3.0$ to -0.5 . The derived stellar parameters for the RPA stars, in LTE and NLTE, are also listed in Table 3.

We derive the NLTE corrections for $[\text{Fe}/\text{H}]$ (denoted as $\Delta[\text{Fe}/\text{H}]$) for the full sample of stars. We plot the results as a function of $[\text{Fe}/\text{H}]_{\text{LTE}}$ in Figure 11. As expected, $\Delta[\text{Fe}/\text{H}]$ increases toward lower metallicities. Such ef-

fects have been shown in multiple previous studies as well (for e.g., Mashonkina et al. 2011; Lind et al. 2012; Bergemann et al. 2012; Amarsi et al. 2016; Ezzeddine et al. 2017). Ezzeddine et al. (2017) derived a linear relation between the NLTE correction for $[\text{Fe}/\text{H}]$, $\Delta[\text{Fe}/\text{H}]$, and $[\text{Fe}/\text{H}](\text{LTE})$ from 20 ultra metal-poor stars with $[\text{Fe}/\text{H}] < -4.0$, such as:

$$\Delta[\text{Fe}/\text{H}] = -0.14[\text{Fe}/\text{H}]_{\text{LTE}} - 0.15 \quad (8)$$

They found that their relationship can also be extended for metal-poor benchmark stars at $-4.0 < [\text{Fe}/\text{H}] < -2.0$. It is therefore useful to re-derive this equation using our full stellar sample analyzed uniformly using LOTUS, for comparison. Following Ezzeddine et al. (2017), we re-derive the relation between $\Delta[\text{Fe}/\text{H}]$ and $[\text{Fe}/\text{H}](\text{LTE})$ using our sample of stars. We re-derive the relation by (i) choosing only the stars with $[\text{Fe}/\text{H}](\text{LTE}) < -0.5$, and (ii) using the stars with $[\text{Fe}/\text{H}](\text{LTE}) < -2.0$. We thus derive $\Delta[\text{Fe}/\text{H}] =$

$$\begin{cases} -0.06(\pm 0.01)[\text{Fe}/\text{H}]_{\text{LTE}} - 0.06(\pm 0.02), \\ \text{for } [\text{Fe}/\text{H}]_{\text{LTE}} < -0.5 \\ -0.16(\pm 0.02)[\text{Fe}/\text{H}]_{\text{LTE}} - 0.32(\pm 0.06), \\ \text{for } [\text{Fe}/\text{H}]_{\text{LTE}} < -2.0 \end{cases} \quad (9)$$

The two relations from these equations for $\Delta[\text{Fe}/\text{H}]$, as well as that derived in Ezzeddine et al. (2017), are shown in Figure 11, fit to our test sample stars from Section 3 as well as the RPA sample. We find that even though the three relations agree within uncertainties (colored bands in Figure 11), they can, however, yield slightly different NLTE corrections depending on the metallicity range for which they were fit. For e.g., our relation derived using stars with $[\text{Fe}/\text{H}] < -2.0$ underestimates the NLTE $[\text{Fe}/\text{H}]$ correction as compared to Ezzeddine et al. (2017) by ~ 0.1 dex at $[\text{Fe}/\text{H}] = -2.0$, while using the relation derived with $[\text{Fe}/\text{H}] <$

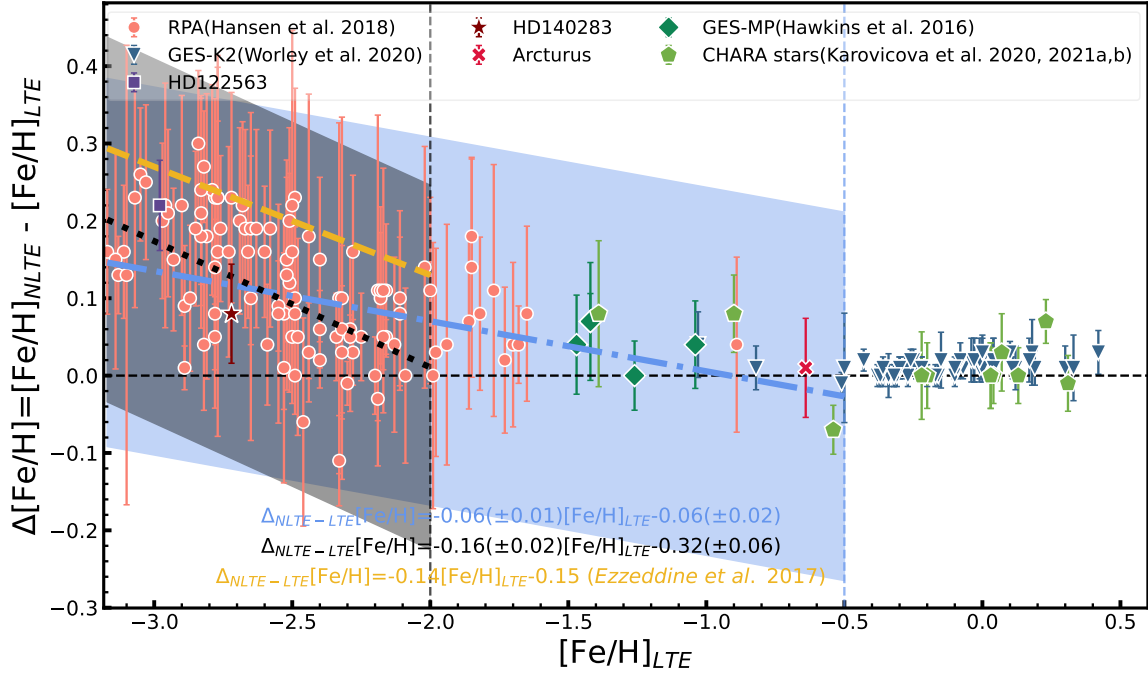


Figure 11. NLTE corrections $\Delta[\text{Fe}/\text{H}]$ versus $[\text{Fe}/\text{H}]_{\text{LTE}}$ determined for this work’s star sample using LOTUS. Different markers indicate stars from different studies as indicated. The Yellow dashed line is a linear fit from Ezzeddine et al. (2017) for stars with $[\text{Fe}/\text{H}] < -4.0$. The Blue dot-dash line is our fit to the stars for $[\text{Fe}/\text{H}] < -0.5$, and the black dotted line is our fit to the stars with $[\text{Fe}/\text{H}] < -2.0$.

-0.5 can underestimate the NLTE correction up to 0.2 dex. This demonstrates that while these relations can provide useful first-order estimates of the NLTE corrections, a complete NLTE analysis (e.g., using LOTUS) is needed for precise estimation of the corrections, as the former can be dependent on the incomplete sample of stars or metallicity range.

Similarly, we derive Δ_{NLTE} corrections for T_{eff} , $\log g$, and v_{mic} for our sample stars. Again, we define the NLTE correction for T_{eff} as $\Delta T_{\text{eff}} = T_{\text{eff}}(\text{NLTE}) - T_{\text{eff}}(\text{LTE})$, for $\log g$ as $\Delta \log g = \log g(\text{NLTE}) - \log g(\text{LTE})$, and for v_{mic} as $\Delta v_{\text{mic}} = v_{\text{mic}}(\text{NLTE}) - v_{\text{mic}}(\text{LTE})$. To best represent these corrections as a function of the other stellar parameters, we divide our sample into box plots grouped into different T_{eff} and $\log g$ bins, as a function of $[\text{Fe}/\text{H}]$ on the x-axis. The results are shown in Figure 12.

In what follows we discuss the NLTE corrections we obtained for each parameter as a function of the other parameters, namely T_{eff} , $\log g$

and $[\text{Fe}/\text{H}]$. We also compare our result to the theoretical NLTE stellar parameter corrections derived by Lind et al. (2012). We note, however, that our comparisons are affected by the fact that our analyzed stars do not cover exactly the same parameter space as theirs, and that our stellar parameters have been derived by LOTUS simultaneously, i.e., taking into account their inter-dependencies, as explained in details in Section 2, whereas Lind et al. (2012) derived their Δ NLTE corrections for each parameter independently, by fixing all the others. As shown in Figure 12, we find that the T_{eff} derived in NLTE are generally higher than those in LTE for very metal-poor ($[\text{Fe}/\text{H}] < -2.5$) supergiants and giant stars ($\log g < 2.0$), with NLTE corrections up to 100 K, whereas lower T_{eff} are obtained in NLTE as compared to LTE as $\log g$ and $[\text{Fe}/\text{H}]$ increases. Lind et al. (2012), who derived their T_{eff} using both excitation and ionization equilibrium by fixing gravity and other stellar parameters in the process. Similarly, they

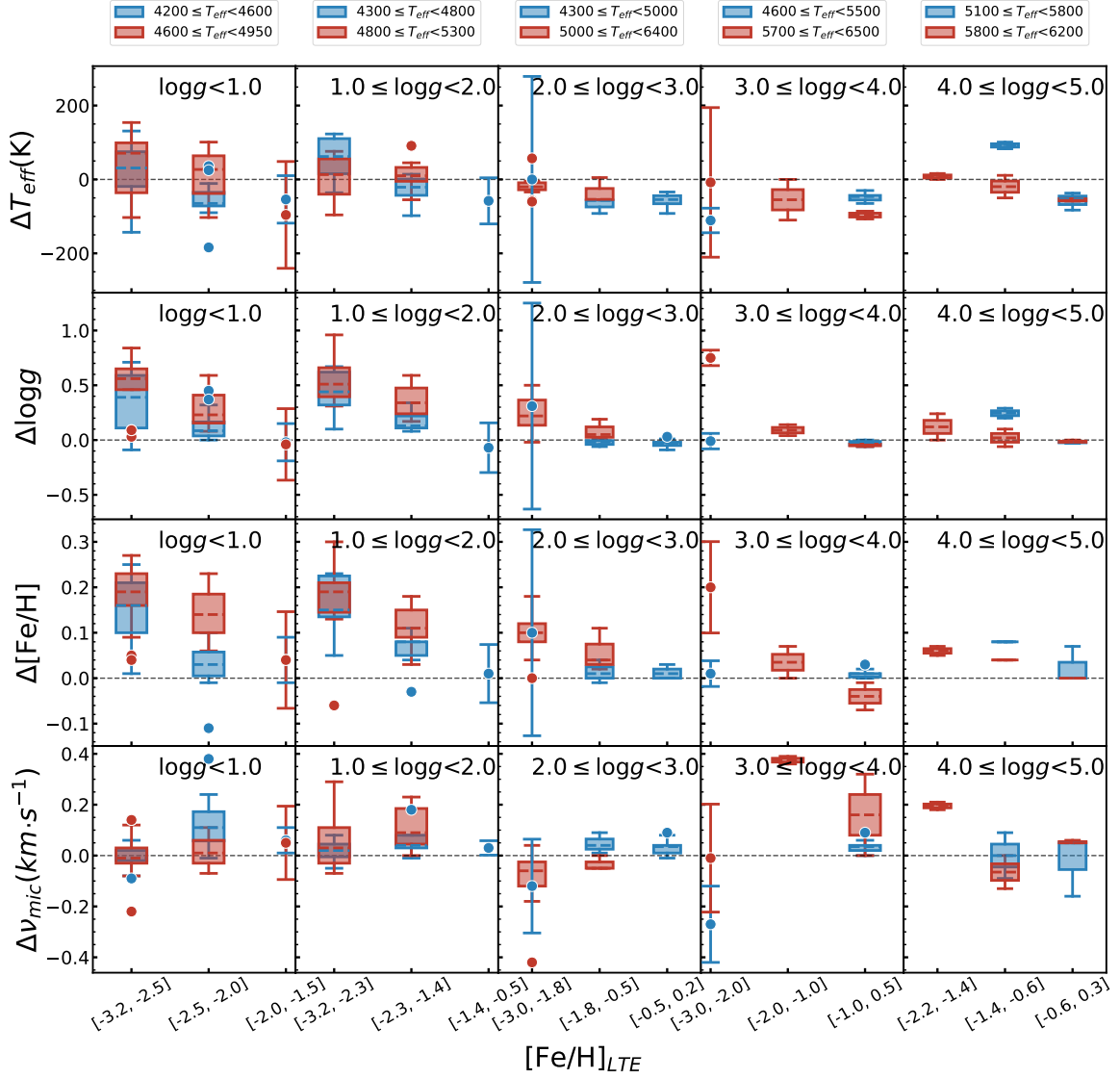


Figure 12. Box plots showing the NLTE corrections of stars considered in this work for stellar parameter T_{eff} , $\log g$, $[\text{Fe}/\text{H}]$, and v_{mic} as derived using LOTUS. Box plots are color-coded for two ranges of T_{eff} for each $\log g$ range, indicated at the top of each column. For intervals with only one star from our sample, boxes are replaced with dots and their error bars.

also restrict their Fe I line transitions to certain cutoffs, choosing only lines with $\text{EP} > 3.5$ eV. They found that their ionization ΔT_{eff} yielded lower LTE T_{eff} as compared to NLTE (see their Figure 5), whereas their excitation ΔT_{eff} yielded negligible positive corrections for $T_{\text{eff}} < 4500$. More pronounced negative corrections were obtained for horizontal branches, supergiants, and extremely metal-poor stars, which are not covered in our sample stars. As noted above, our derived T_{eff} using LOTUS implement the contri-

bution from both excitation and ionization equilibrium, by taking into account their $T_{\text{eff}}\text{-}\log g$ inter-dependencies. In that context, a thorough comparison of our ΔT_{eff} results to either excitation or ionization theoretical corrections derived by Lind et al. (2012) are not very useful, however, similar to their results we generally find that the NLTE corrections for the bulk of our stars are affected by less than 50 K (and up to 100 K) in the considered parameter range, which is within our derived uncertainties.

We also derive $\Delta \log g$ for our sample stars. As expected, the NLTE corrections for $\log g$ increase towards lower gravities, lower metallicities, and higher temperatures. On average, our corrections are $\sim +0.3 - 0.5$ for $[\text{Fe}/\text{H}] < -2.0$, $\sim +0.1 - 0.3$ for $-2.0 < [\text{Fe}/\text{H}] < -1.0$, for giants and supergiant stars with $\log g < 2.0$, with outliers reaching up to 1.0 dex. For stars with $\log g > 2.0$, the NLTE corrections can be up to ~ 0.3 depending on metallicities. These results broadly agree with the theoretical corrections derived in Lind et al. (2012). It can thus be concluded that LTE analyses can strongly underestimate the surface gravities of stars, particularly for warmer metal-poor giants, and should thus be reliably derived in NLTE for reliable consequent stellar population analyses.

Finally, the NLTE corrections for v_{mic} are generally small and are within 2.0 km s^{-1} from those derived in LTE. The corrections are mainly positive for lower metallicity giants and supergiant stars, as in particular their Fe I lines are more strongly affected by NLTE, which leads to lower microturbulent velocities in LTE as compared to NLTE. Our results are generally consistent with the Δv_{mic} derived by Lind et al. (2012) from their theoretical models.

5. CAVEATS

We have so far described and demonstrated that LOTUS can be used as a reliable tool to derive NLTE and LTE atmospheric stellar parameters. There are, however, some caveats that warrant pointing out which can affect the results, particularly for stars occupying certain parameter spaces in our grids.

EW Interpolation—A key component of LOTUS is the interpolation module that expresses the EWs as a function of stellar parameters, using the generalized curve of growth (GCOG). As explained in Section 2.3.1, we conduct thorough tests to choose the best polynomial interpolator to calculate the GCOG for each spectral

type. However, some polynomial models cannot reliably fit the GCOG to derive Fe I and Fe II for certain lines at some parameter regions. For example, the Fe I line at 3608.86 \AA with $EP=1.01 \text{ eV}$, shows a difference between theoretic computed NLTE EW directly using MULTI2.3 and LOTUS interpolated NLTE EW of 20 m\AA at $T_{\text{eff}}=4000$ and $[\text{Fe}/\text{H}] = -0.5$, while the same value can be as low as 5 m\AA at the same T_{eff} with $[\text{Fe}/\text{H}] = -3.5$. Thus, for those models, the iron abundances derived from the interpolated polynomial models can deviate up to 0.5 dex in abundances from those outputs directly from MULTI2.3 (i.e, non interpolated EWs). Such large offsets are due to the EWs of those lines not being sensitive to the variation of atmospheric stellar parameters, or being too small (close to zero) at most atmospheric stellar parameters. In other words, those lines are uncertain to determine iron abundances from at those parameter ranges. We emphasize that the number of those lines are limited and do not impact the statistical properties of interpolated performance for all lines we consider in the linelist, as shown in Figure 4. We do not drop these lines from our final linelist in Table 2 as the uncertainties can only affect a few Fe I lines in a limited part of the parameter space, which are then normally automatically excluded as outliers in the final optimization during sigma clipping. In future LOTUS updates, we plan to perform more detailed investigation into what parameter regions these lines occupy and how to improve interpolation of EW for these lines in the code.

Number of lines—The derived atmospheric stellar parameters using LOTUS can be affected by the number of Fe I and Fe II used in the optimization. In Figure 13, we show the effects of the uncertainties derived for each stellar parameter as a function of the number of Fe I and Fe II lines used in LOTUS. We find that the uncertainties on the derived parameters decrease as

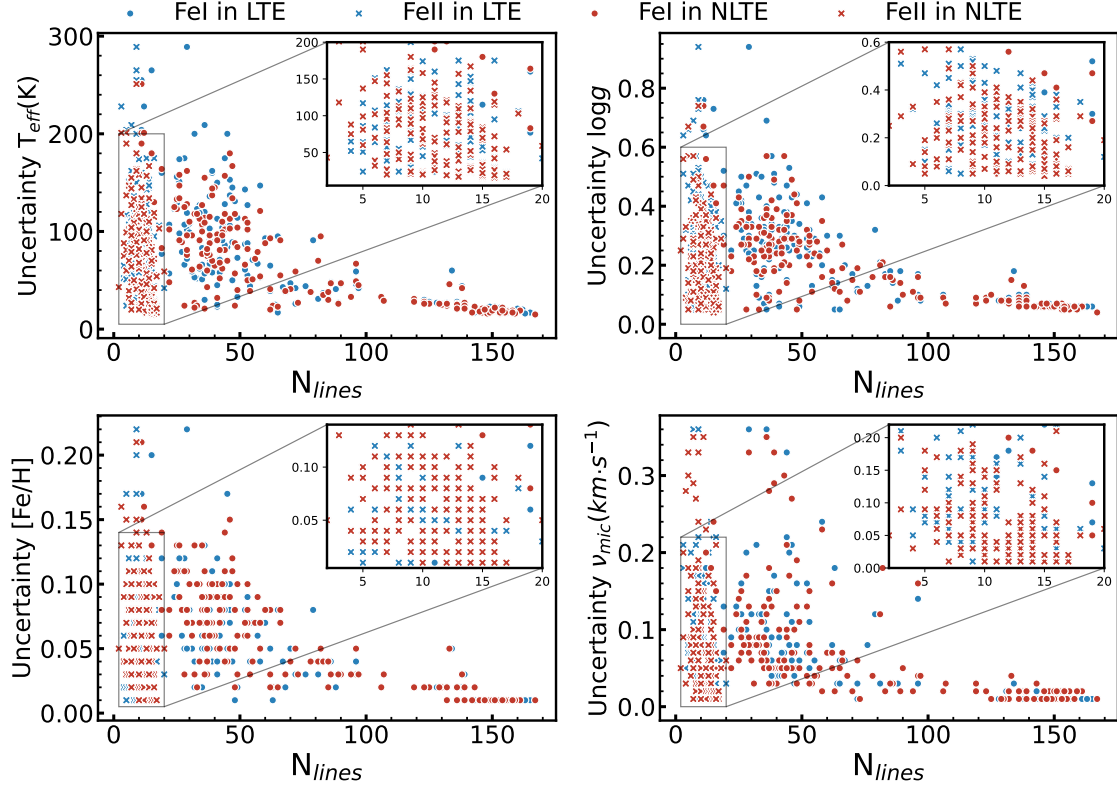


Figure 13. Uncertainties of the derived atmospheric stellar parameters of the stars considered in this work versus the number of iron lines color-coded for LTE (blue) and NLTE (red), respectively. Empty circles correspond to Fe I lines and crosses for Fe II lines. Close-up inset plots show the inner close region where most of the Fe II lines are.

a function of increasing the number of Fe I and Fe II lines and are much more strongly affected by the number of Fe I lines, N_{FeI} in particular. For $N_{\text{lines}} > 140$, the uncertainty on T_{eff} and $\log g$ are less than 50 K and 0.1 dex, respectively, however can reach up to 200 K and 0.6 dex for $N_{\text{lines}} < 50$. We thus recommend that users input more than at least 50 lines in LOTUS for reliable results. Additionally, as the number of Fe II lines detected in cool FGK stellar spectra are much smaller than the Fe I lines (on the order of 10-30, depending on the $[\text{Fe}/\text{H}]$ of the star), we moreover recommend that users try to maximize the number of Fe II lines they can measure the EW for in their stars, as that will increase the precision of the parameter determination. In future work we plan to test LOTUS on lower resolution spectroscopic observations, as well as

simultaneous high-resolution data for the same stars for comparison, to accurately quantify the effects of the spectral resolution on the results derived by LOTUS.

K-type stars—The atmospheric stellar parameters, particularly $\log g$, derived for K-type stars using LOTUS can have larger uncertainties than other spectra types. Tsantaki et al. (2019) noted that $\log g$ determined for K-type stars using ionization balance between Fe I and Fe II lines might be underestimated depending on the choice of Fe II lines in the optimization. They argued that the derived $\log g$ can strongly depend on the choice of Fe II lines and thus must be thoroughly selected. We investigated this effect on our GES-K2 sample, in which most of our stars are K-type giants or sub-giants. We

find that both our NLTE and LTE results can overestimate the surface gravity by up to 0.1 to 0.13 dex as compared to asteroseismic values, depending on the selection of Fe II lines.

3D models—Since our atmospheric stellar models are limited to 1D, inferred iron abundances might suffer from 3D effects including the effects of atmospheric inhomogeneities and horizontal radiation transfer, as well as the effect of differences in the mean temperature stratification [Amarsi et al. \(2016\)](#). These can underestimate the abundances inferred from Fe I and Fe II roughly by up to 0.1 dex in 1D, NLTE as compared with Fe abundances derived using 3D, NLTE. Such effects are more strongly pronounced for Fe II lines than Fe I as explained in [Amarsi et al. \(2016\)](#). We find that adding a 0.1 dex correction for our 1D, NLTE $[\text{Fe}/\text{H}]$ for HD122563 brings it closer to the 3D, NLTE $[\text{Fe}/\text{H}]$ derived in ([Amarsi et al. 2016](#)). On the other hand, a 0.22 dex difference to [Amarsi et al. \(2016\)](#) is still present when adding such correction to the $[\text{Fe}/\text{H}]$ for HD140283. This can be due to stellar parameter differences between both studies, as well as different adopted Fe I and Fe II linelists. Nevertheless, we note that a 0.1 3D correction can be smaller than the NLTE corrections obtained for $[\text{Fe}/\text{H}]$, especially for low metallicity stars, which can reach up to 0.3 dex for $[\text{Fe}/\text{H}]=-3.0$.

6. SUMMARY & CONCLUSIONS

We present the open-source code, LOTUS, developed to automatically derive fast and precise atmospheric stellar parameters (T_{eff} , $\log g$, $[\text{Fe}/\text{H}]$ and v_{mic}) of stars in 1D, LTE, and 1D, NLTE using Fe I and Fe II equivalent width measurement from stellar spectra as input.

LOTUS implements a generalized curve of growth (GCOG) method to derive abundances from a pre-computed grid of theoretical EWs in a high-resolution and dense spectral parameter space. The GCOG takes into account the EW



dependencies of every Fe I and Fe II line on the corresponding atmospheric stellar parameters. A global differential evolution optimization algorithm, optimized to the spectral type of the star, is then used to derive the fundamental stellar parameters. In addition, LOTUS can be used to estimate precise uncertainties for each stellar parameter using a well-tested Markov Chain Monte Carlo (MCMC) algorithm.

We tested our code on several benchmark stars and stellar samples with reliable non-spectroscopic (asteroseismic, photometric, and interferometric) measurements for a wide range of parameter space typical of FGK stars. We find that our NLTE-derived stellar parameters for T_{eff} and $\log g$ using LOTUS are within 30 K and 0.2 dex for benchmark stars including the metal-poor standard stars, HD140283 and HD122563, as well as Arcturus. We also test LOTUS on a large sample of *Gaia*-ESO (GES) dwarf stars from [Hawkins et al. \(2016\)](#) and GES-K2 with asteroseismic gravities from K2, as well as stars with CHARA interferometric observations. Similarly, we find that LOTUS performs very well in reproducing the non-spectroscopic T_{eff} and $\log g$ within the mean of sample as < 20 K and < 0.1 dex in NLTE, and to within ~ 70 K and ~ 0.2 dex in LTE.

We also apply LOTUS on a large sample of metal-poor stars from the R-Process Alliance (RPA, [Hansen et al. 2018](#)). We use the RPA sample as well as the test sample stars to derive NLTE stellar parameter corrections for our stars and review the $\Delta[\text{Fe}/\text{H}]$ versus $[\text{Fe}/\text{H}](\text{LTE})$ relation derived in [Ezzeddine et al. \(2017\)](#). We find that our NLTE corrections agree with theoretical corrections investigated by [Lind et al. \(2012\)](#).

We test LOTUS thoroughly for performance for different spectral types and parameter spaces. We find that despite some caveats discussed in Section 5, LOTUS can overall be reliably used to provide fast and accurate NLTE derivation

for a wide range of stellar parameters, especially metal-poor giants which can be strongly affected by deviations from LTE. We thus strongly recommend that the community use it to apply for the spectroscopic analyses of stars and stellar populations.

We provide open community access to LOTUS, as well as the pre-computed interpolated LTE and NLTE EW grids available on Github , with documentation and working examples on Readthedocs .

ACKNOWLEDGMENTS

We thank the anonymous referee for their useful comments that improved the manuscript. R.E. acknowledges support from JINA-CEE (Joint Institute for Nuclear Astrophysics - Center for the Evolution of the Elements), funded by the NSF under Grant No. PHY-1430152. The authors acknowledge the University of Florida Research Computing for providing computational resources and support that have contributed to the research results reported in this publication. URL: [UFRC](#).

Software: `astropy` (Astropy Collaboration et al. 2013, 2018), `numpy` (van der Walt et al. 2011; Harris et al. 2020), `pandas` (pandas development team 2020), `scikit-learn` (Buitinck et al. 2013), `scipy` (Virtanen et al. 2020), `sympy` (Meurer et al. 2017), `matplotlib` (Hunter 2007), `h5py` (Collette 2013), `PyMC3` (Salvatier et al. 2016), `theano` (Team et al. 2016), `corner` (Foreman-Mackey 2016), `numdifftools` (Brodtkorb & D’Errico 2015)

APPENDIX

A. LINELIST OF Fe I AND Fe II IN LOTUS

Table 2. Fe I and Fe II linelist selected for LOTUS (see Section 2.1.4 for details)

Species	$\lambda(\text{\AA})$	$E_{low}(\text{ev})$	$\log gf$
Fe I	3440.61	0.00	-0.67
Fe I	3440.99	0.05	-0.96
Fe I	3447.28	2.20	-1.02
Fe I	3450.33	2.22	-0.90
Fe I	3451.91	2.22	-1.00
Fe I	3476.70	0.12	-1.51
Fe I	3490.57	0.05	-1.10
Fe I	3497.84	0.11	-1.55
Fe I	3540.12	2.87	-0.71
Fe I	3565.38	0.96	-0.13
Fe I	3608.86	1.01	-0.10
Fe I	3618.77	0.99	-0.00
Fe I	3647.84	0.92	-0.19
Fe I	3689.46	2.94	-0.17
Fe I	3719.93	0.00	-0.43
Fe I	3727.62	0.96	-0.63
Fe I	3742.62	2.94	-0.81
Fe I	3758.23	0.96	-0.03
Fe I	3763.79	0.99	-0.24
Fe I	3765.54	3.24	0.48
Fe I	3786.68	1.01	-2.22
Fe I	3787.88	1.01	-0.86
Fe I	3805.34	3.30	0.31
Fe I	3808.73	2.56	-1.17
Fe I	3815.84	1.48	0.23
Fe I	3820.43	0.86	0.12
Fe I	3825.88	0.91	-0.04
Fe I	3827.82	1.56	0.06
Fe I	3840.44	0.99	-0.51
Fe I	3841.05	1.61	-0.04
Fe I	3849.97	1.01	-0.87
Fe I	3856.37	0.05	-1.29

Table 2 *continued***Table 2** (*continued*)

Species	$\lambda(\text{\AA})$	$E_{low}(\text{ev})$	$\log gf$
Fe I	3865.52	1.01	-0.98
Fe I	3878.02	0.96	-0.91
Fe I	3895.66	0.11	-1.67
Fe I	3899.71	0.09	-1.53
Fe I	3902.95	1.56	-0.47
Fe I	3920.26	0.12	-1.75
Fe I	3922.91	0.05	-1.65
Fe I	3949.95	2.18	-1.25
Fe I	3977.74	2.20	-1.12
Fe I	4005.24	1.56	-0.61
Fe I	4045.81	1.49	0.28
Fe I	4058.22	3.21	-1.18
Fe I	4063.59	1.56	0.06
Fe I	4067.98	3.21	-0.53
Fe I	4070.77	3.24	-0.87
Fe I	4071.74	1.61	-0.02
Fe I	4114.44	2.83	-1.30
Fe I	4132.06	1.61	-0.68
Fe I	4134.68	2.83	-0.65
Fe I	4143.87	1.56	-0.51
Fe I	4147.67	1.49	-2.10
Fe I	4150.25	3.43	-1.19
Fe I	4154.50	2.83	-0.69
Fe I	4156.80	2.83	-0.81
Fe I	4157.78	3.42	-0.40
Fe I	4158.79	3.43	-0.70
Fe I	4174.91	0.91	-2.97
Fe I	4175.64	2.85	-0.83
Fe I	4181.76	2.83	-0.37
Fe I	4182.38	3.02	-1.18
Fe I	4184.89	2.83	-0.87
Fe I	4187.04	2.45	-0.56
Fe I	4187.80	2.42	-0.55
Fe I	4191.43	2.47	-0.67

Table 2 *continued*

Table 2 (*continued*)

Species	$\lambda(\text{\AA})$	$E_{low}(\text{ev})$	loggf
Fe I	4195.33	3.33	-0.49
Fe I	4199.10	3.05	0.16
Fe I	4202.03	1.49	-0.71
Fe I	4216.18	0.00	-3.36
Fe I	4217.55	3.43	-0.48
Fe I	4222.21	2.45	-0.97
Fe I	4227.43	3.33	0.27
Fe I	4233.60	2.48	-0.60
Fe I	4238.81	3.40	-0.23
Fe I	4250.12	2.47	-0.41
Fe I	4250.79	1.56	-0.71
Fe I	4260.47	2.40	0.08
Fe I	4271.15	2.45	-0.35
Fe I	4271.76	1.49	-0.16
Fe I	4282.40	2.18	-0.78
Fe I	4325.76	1.61	0.01
Fe I	4352.73	2.22	-1.29
Fe I	4375.93	0.00	-3.03
Fe I	4388.41	3.60	-0.68
Fe I	4404.75	1.56	-0.14
Fe I	4415.12	1.61	-0.62
Fe I	4427.31	0.05	-3.04
Fe I	4430.61	2.22	-1.66
Fe I	4432.57	3.57	-1.58
Fe I	4442.34	2.20	-1.25
Fe I	4443.19	2.86	-1.04
Fe I	4447.72	2.22	-1.36
Fe I	4461.65	0.09	-3.21
Fe I	4466.55	2.83	-0.60
Fe I	4484.22	3.60	-0.64
Fe I	4489.74	0.12	-3.97
Fe I	4494.56	2.20	-1.14
Fe I	4514.18	3.05	-1.96
Fe I	4531.15	1.48	-2.16
Fe I	4547.85	3.55	-0.82
Fe I	4574.22	3.21	-2.35
Fe I	4592.65	1.56	-2.45
Fe I	4595.36	3.30	-1.76

Table 2 *continued***Table 2** (*continued*)

Species	$\lambda(\text{\AA})$	$E_{low}(\text{ev})$	loggf
Fe I	4602.00	1.61	-3.15
Fe I	4602.94	1.49	-2.22
Fe I	4607.65	3.27	-1.33
Fe I	4619.29	3.60	-1.06
Fe I	4630.12	2.28	-2.58
Fe I	4637.50	3.28	-1.29
Fe I	4643.46	3.65	-1.15
Fe I	4647.43	2.95	-1.35
Fe I	4661.97	2.99	-2.50
Fe I	4668.13	3.27	-1.08
Fe I	4704.95	3.69	-1.32
Fe I	4733.59	1.49	-2.99
Fe I	4736.77	3.21	-0.67
Fe I	4786.81	3.02	-1.61
Fe I	4787.83	3.00	-2.62
Fe I	4788.76	3.24	-1.763
Fe I	4789.65	3.55	-0.96
Fe I	4793.96	3.05	-3.43
Fe I	4794.35	2.42	-3.95
Fe I	4800.65	4.14	-1.03
Fe I	4802.88	3.64	-1.51
Fe I	4807.71	3.37	-2.15
Fe I	4808.15	3.25	-2.69
Fe I	4869.46	3.55	-2.42
Fe I	4871.32	2.87	-0.34
Fe I	4872.14	2.88	-0.57
Fe I	4873.75	3.30	-2.96
Fe I	4875.88	3.33	-1.90
Fe I	4877.60	3.00	-3.05
Fe I	4882.14	3.42	-1.48
Fe I	4885.43	3.88	-0.97
Fe I	4890.76	2.88	-0.38
Fe I	4891.49	2.85	-0.11
Fe I	4896.44	3.88	-1.89
Fe I	4903.31	2.88	-0.89
Fe I	4905.13	3.93	-1.73
Fe I	4907.73	3.43	-1.70
Fe I	4910.02	3.40	-1.28

Table 2 *continued*

Table 2 (*continued*)

Species	$\lambda(\text{\AA})$	$E_{low}(\text{ev})$	loggf
Fe I	4911.78	3.93	-1.75
Fe I	4918.99	2.86	-0.34
Fe I	4920.50	2.83	0.07
Fe I	4924.77	2.28	-2.11
Fe I	4938.81	2.88	-1.08
Fe I	4939.69	0.86	-3.34
Fe I	4946.39	3.37	-1.11
Fe I	4950.11	3.42	-1.49
Fe I	4962.57	4.18	-1.18
Fe I	4966.09	3.33	-0.79
Fe I	4969.92	4.22	-0.71
Fe I	4985.55	2.87	-1.33
Fe I	4992.79	4.26	-2.35
Fe I	4994.13	0.92	-3.08
Fe I	4999.11	4.19	-1.64
Fe I	5001.86	3.88	-0.01
Fe I	5002.79	3.40	-1.46
Fe I	5005.71	3.88	-0.12
Fe I	5006.12	2.83	-0.61
Fe I	5012.69	4.28	-1.69
Fe I	5014.94	3.94	-0.18
Fe I	5022.24	3.98	-0.33
Fe I	5023.19	4.28	-1.50
Fe I	5028.13	3.57	-1.02
Fe I	5039.25	3.37	-1.52
Fe I	5044.21	2.85	-2.02
Fe I	5048.44	3.96	-1.00
Fe I	5049.82	2.28	-1.35
Fe I	5051.63	0.92	-2.80
Fe I	5054.64	3.64	-1.92
Fe I	5058.50	3.64	-2.83
Fe I	5060.08	0.00	-5.43
Fe I	5068.77	2.94	-1.04
Fe I	5079.22	2.20	-2.07
Fe I	5079.74	0.99	-3.22
Fe I	5083.34	0.96	-2.96
Fe I	5088.15	4.15	-1.68
Fe I	5107.45	0.99	-3.09

Table 2 *continued***Table 2** (*continued*)

Species	$\lambda(\text{\AA})$	$E_{low}(\text{ev})$	loggf
Fe I	5107.64	1.56	-2.36
Fe I	5109.65	4.30	-0.98
Fe I	5115.78	3.57	-2.64
Fe I	5123.72	1.01	-3.07
Fe I	5127.36	0.92	-3.31
Fe I	5131.47	2.22	-2.52
Fe I	5133.69	4.18	0.36
Fe I	5141.74	2.42	-2.24
Fe I	5150.84	0.99	-3.04
Fe I	5151.91	1.01	-3.32
Fe I	5166.28	0.00	-4.20
Fe I	5171.60	1.49	-1.79
Fe I	5191.45	3.04	-0.55
Fe I	5192.34	3.00	-0.42
Fe I	5194.94	1.56	-2.09
Fe I	5197.94	4.30	-1.54
Fe I	5198.71	2.22	-2.13
Fe I	5202.34	2.18	-1.84
Fe I	5215.18	3.27	-0.86
Fe I	5216.27	1.61	-2.15
Fe I	5217.39	3.21	-1.07
Fe I	5223.18	3.63	-1.78
Fe I	5225.53	0.11	-4.79
Fe I	5228.38	4.22	-1.19
Fe I	5232.94	2.94	-0.06
Fe I	5242.49	3.63	-0.97
Fe I	5243.78	4.26	-1.05
Fe I	5247.05	0.09	-4.95
Fe I	5250.21	0.12	-4.93
Fe I	5250.65	2.20	-2.18
Fe I	5253.02	2.28	-3.84
Fe I	5253.46	3.28	-1.58
Fe I	5262.88	3.25	-2.56
Fe I	5263.31	3.27	-0.87
Fe I	5266.56	3.00	-0.39
Fe I	5281.79	3.04	-0.83
Fe I	5283.62	3.24	-0.52
Fe I	5285.13	4.43	-1.66

Table 2 *continued*

Table 2 (*continued*)

Species	$\lambda(\text{\AA})$	$E_{low}(\text{ev})$	$\log gf$
Fe I	5288.52	3.69	-1.49
Fe I	5293.96	4.14	-1.77
Fe I	5294.55	3.64	-2.76
Fe I	5295.31	4.42	-1.59
Fe I	5300.40	4.59	-1.65
Fe I	5302.30	3.28	-0.74
Fe I	5307.36	1.61	-2.99
Fe I	5321.11	4.43	-1.09
Fe I	5322.04	2.28	-2.80
Fe I	5324.18	3.21	-0.11
Fe I	5332.90	1.56	-2.78
Fe I	5339.93	3.27	-0.63
Fe I	5341.02	1.61	-1.95
Fe I	5364.87	4.45	0.23
Fe I	5365.40	3.57	-1.02
Fe I	5367.47	4.42	0.44
Fe I	5369.96	4.37	0.54
Fe I	5371.49	0.96	-1.64
Fe I	5373.71	4.47	-0.71
Fe I	5379.57	3.69	-1.42
Fe I	5383.37	4.31	0.65
Fe I	5386.33	4.15	-1.67
Fe I	5389.48	4.42	-0.41
Fe I	5395.22	4.45	-2.07
Fe I	5397.13	0.92	-1.99
Fe I	5398.28	4.45	-0.63
Fe I	5405.77	0.99	-1.85
Fe I	5410.91	4.47	0.4
Fe I	5412.78	4.43	-1.72
Fe I	5415.20	4.39	0.64
Fe I	5417.03	4.42	-1.58
Fe I	5424.07	4.32	0.52
Fe I	5429.70	0.96	-1.88
Fe I	5434.52	1.01	-2.12
Fe I	5436.59	2.28	-2.96
Fe I	5441.34	4.31	-1.63
Fe I	5445.04	4.39	-0.02
Fe I	5461.55	4.45	-1.8

Table 2 *continued***Table 2** (*continued*)

Species	$\lambda(\text{\AA})$	$E_{low}(\text{ev})$	$\log gf$
Fe I	5464.28	4.14	-1.40
Fe I	5466.40	4.37	-0.63
Fe I	5470.09	4.45	-1.71
Fe I	5473.90	4.15	-0.72
Fe I	5483.10	4.15	-1.39
Fe I	5487.15	4.42	-1.43
Fe I	5491.83	4.19	-2.19
Fe I	5493.50	4.10	-1.48
Fe I	5494.46	4.08	-1.99
Fe I	5497.52	1.01	-2.85
Fe I	5501.47	0.96	-3.05
Fe I	5506.78	0.99	-2.80
Fe I	5522.45	4.21	-1.45
Fe I	5525.54	4.23	-1.08
Fe I	5536.58	2.83	-3.71
Fe I	5539.28	3.64	-2.56
Fe I	5543.94	4.22	-1.04
Fe I	5546.51	4.37	-1.21
Fe I	5552.69	4.95	-1.89
Fe I	5554.90	4.55	-0.27
Fe I	5560.21	4.43	-1.09
Fe I	5563.60	4.19	-0.75
Fe I	5569.62	3.42	-0.52
Fe I	5576.09	3.43	-0.90
Fe I	5586.76	3.37	-0.11
Fe I	5587.57	4.14	-1.75
Fe I	5618.63	4.21	-1.25
Fe I	5619.60	4.39	-1.60
Fe I	5624.02	4.39	-1.38
Fe I	5624.54	3.42	-0.76
Fe I	5633.95	4.99	-0.23
Fe I	5635.82	4.26	-1.79
Fe I	5636.70	3.64	-2.51
Fe I	5638.26	4.22	-0.72
Fe I	5641.43	4.26	-1.08
Fe I	5649.99	5.10	-0.82
Fe I	5651.47	4.47	-1.90
Fe I	5652.32	4.26	-1.85

Table 2 *continued*

Table 2 (*continued*)

Species	$\lambda(\text{\AA})$	$E_{low}(\text{ev})$	loggf
Fe I	5653.87	4.39	-1.54
Fe I	5655.18	5.06	-0.60
Fe I	5661.35	4.28	-1.76
Fe I	5662.52	4.18	-0.41
Fe I	5667.52	4.18	-1.58
Fe I	5679.02	4.65	-0.82
Fe I	5686.53	4.55	-0.45
Fe I	5691.50	4.30	-1.45
Fe I	5696.09	4.55	-1.72
Fe I	5698.02	3.64	-2.58
Fe I	5701.54	2.56	-2.22
Fe I	5705.46	4.30	-1.35
Fe I	5731.76	4.26	-1.20
Fe I	5732.30	4.99	-1.46
Fe I	5741.85	4.26	-1.67
Fe I	5742.96	4.18	-2.41
Fe I	5753.12	4.26	-0.62
Fe I	5760.34	3.64	-2.39
Fe I	5775.08	4.22	-1.08
Fe I	5778.45	2.59	-3.43
Fe I	5784.66	3.40	-2.55
Fe I	5816.37	4.55	-0.60
Fe I	5835.10	4.26	-2.27
Fe I	5837.70	4.29	-2.24
Fe I	5838.37	3.94	-2.24
Fe I	5849.68	3.69	-2.89
Fe I	5853.15	1.49	-5.18
Fe I	5855.08	4.61	-1.48
Fe I	5858.78	4.22	-2.16
Fe I	5883.82	3.96	-1.26
Fe I	5902.47	4.59	-1.71
Fe I	5905.67	4.65	-0.69
Fe I	5916.25	2.45	-2.99
Fe I	5927.79	4.65	-0.99
Fe I	5929.68	4.55	-1.31
Fe I	5930.18	4.65	-0.23
Fe I	5934.65	3.93	-1.07
Fe I	5940.99	4.18	-2.05

Table 2 *continued***Table 2** (*continued*)

Species	$\lambda(\text{\AA})$	$E_{low}(\text{ev})$	loggf
Fe I	5956.69	0.86	-4.60
Fe I	6003.01	3.88	-1.10
Fe I	6008.56	3.88	-0.98
Fe I	6012.21	2.22	-4.04
Fe I	6024.06	4.55	-0.12
Fe I	6027.05	4.08	-1.09
Fe I	6056.00	4.73	-0.32
Fe I	6065.48	2.61	-1.53
Fe I	6079.01	4.65	-1.02
Fe I	6082.71	2.22	-3.58
Fe I	6093.64	4.61	-1.40
Fe I	6094.37	4.65	-1.84
Fe I	6096.66	3.98	-1.83
Fe I	6120.25	0.91	-5.97
Fe I	6127.91	4.14	-1.40
Fe I	6136.61	2.45	-1.40
Fe I	6136.99	2.20	-2.95
Fe I	6137.69	2.59	-1.40
Fe I	6151.62	2.18	-3.30
Fe I	6165.36	4.14	-1.47
Fe I	6173.33	2.22	-2.88
Fe I	6187.99	3.94	-1.62
Fe I	6191.56	2.43	-1.42
Fe I	6200.31	2.61	-2.43
Fe I	6213.43	2.22	-2.48
Fe I	6219.28	2.20	-2.43
Fe I	6226.73	3.88	-2.12
Fe I	6229.23	2.85	-2.81
Fe I	6230.72	2.56	-1.28
Fe I	6232.64	3.65	-1.24
Fe I	6240.65	2.22	-3.17
Fe I	6246.32	3.60	-0.77
Fe I	6252.56	2.40	-1.69
Fe I	6265.13	2.18	-2.55
Fe I	6270.22	2.86	-2.47
Fe I	6271.28	3.33	-2.70
Fe I	6297.79	2.22	-2.74
Fe I	6301.50	3.65	-0.71

Table 2 *continued*

Table 2 (*continued*)

Species	$\lambda(\text{\AA})$	$E_{low}(\text{ev})$	$\log gf$
Fe I	6315.81	4.08	-1.63
Fe I	6322.69	2.59	-2.43
Fe I	6330.85	4.73	-1.64
Fe I	6335.33	2.20	-2.18
Fe I	6336.82	3.69	-0.85
Fe I	6338.88	4.80	-0.96
Fe I	6344.15	2.43	-2.92
Fe I	6355.03	2.84	-2.29
Fe I	6364.36	4.80	-1.33
Fe I	6380.74	4.19	-1.38
Fe I	6393.60	2.43	-1.58
Fe I	6400.32	0.91	-4.32
Fe I	6408.02	3.69	-0.99
Fe I	6411.65	3.65	-0.59
Fe I	6421.35	2.28	-2.03
Fe I	6430.85	2.18	-2.01
Fe I	6475.62	2.56	-2.94
Fe I	6481.87	2.28	-2.98
Fe I	6494.98	2.40	-1.27
Fe I	6496.47	4.80	-0.53
Fe I	6498.94	0.96	-4.69
Fe I	6518.37	2.83	-2.44
Fe I	6533.93	4.56	-1.36
Fe I	6546.24	2.76	-1.54
Fe I	6569.21	4.73	-0.38
Fe I	6574.23	0.99	-5.00
Fe I	6592.91	2.73	-1.47
Fe I	6593.87	2.43	-2.42
Fe I	6597.56	4.80	-0.97
Fe I	6609.11	2.56	-2.69
Fe I	6627.54	4.55	-1.59
Fe I	6648.08	1.01	-5.92
Fe I	6677.99	2.69	-1.42
Fe I	6699.14	4.59	-2.10
Fe I	6703.57	2.76	-3.06
Fe I	6713.74	4.80	-1.50
Fe I	6733.15	4.64	-1.15
Fe I	6739.52	1.56	-4.79

Table 2 *continued***Table 2** (*continued*)

Species	$\lambda(\text{\AA})$	$E_{low}(\text{ev})$	$\log gf$
Fe I	6750.15	2.42	-2.62
Fe I	6752.71	4.64	-1.20
Fe I	6786.86	4.19	-1.97
Fe I	6804.27	4.58	-1.81
Fe I	6806.84	2.73	-2.13
Fe I	6810.26	4.61	-0.99
Fe I	6820.37	4.64	-1.22
Fe I	6843.66	4.55	-0.73
Fe I	6855.16	4.56	-0.49
Fe I	6858.15	4.61	-0.90
Fe I	6978.85	2.48	-2.50
Fe I	7495.07	4.22	-0.10
Fe I	7511.02	4.18	0.12
Fe I	7568.90	4.28	-0.88
Fe I	8220.38	4.32	0.30
Fe II	4173.45	2.58	-2.38
Fe II	4178.86	2.58	-2.51
Fe II	4233.16	2.58	-2.02
Fe II	4303.17	2.70	-2.52
Fe II	4385.38	2.78	-2.64
Fe II	4416.82	2.78	-2.57
Fe II	4491.40	2.86	-2.71
Fe II	4508.28	2.86	-2.42
Fe II	4515.34	2.84	-2.60
Fe II	4522.63	2.84	-2.29
Fe II	4549.47	2.83	-1.92
Fe II	4555.89	2.83	-2.40
Fe II	4576.33	2.84	-2.95
Fe II	4583.83	2.81	-1.94
Fe II	4620.51	2.83	-3.21
Fe II	4923.93	2.89	-1.26
Fe II	4993.35	2.81	-3.68
Fe II	5197.57	3.23	-2.22
Fe II	5234.63	3.22	-2.18
Fe II	5256.93	2.89	-4.18
Fe II	5264.80	3.23	-3.13
Fe II	5276.00	3.20	-2.01
Fe II	5316.61	3.15	-1.87

Table 2 *continued*

Table 2 (*continued*)

Species	$\lambda(\text{\AA})$	$E_{low}(\text{ev})$	$\text{logg}f$
Fe II	5316.78	3.22	-2.74
Fe II	5325.55	3.22	-3.16
Fe II	5414.07	3.22	-3.58
Fe II	5425.25	3.20	-3.22
Fe II	5534.84	3.25	-2.80
Fe II	5991.37	3.15	-3.65
Fe II	6084.10	3.20	-3.88
Fe II	6113.32	3.22	-4.23

Fe II	6149.24	3.89	-2.84
Fe II	6247.56	3.89	-2.44
Fe II	6369.46	2.89	-4.11
Fe II	6432.68	2.89	-3.57
Fe II	6456.38	3.90	-2.19

B. DERIVED STELLAR PARAMETERS OF THE TARGET STARS IN THIS WORK

Table 3. Derived Stellar Atmospheric Parameters of the Target Stars

Star Name	LTE					NLTE						
	T_{eff} (K)	$\log g$ (cgs)	[Fe/H] (dex)	v_{mic} (km s ⁻¹)	N_{FeI}	$\chi_{\text{FeI,cutoff}}$ (ev)	T_{eff} (K)	$\log g$ (cgs)	[Fe/H] (dex)	v_{mic} (km s ⁻¹)	N_{FeII}	$\chi_{\text{FeI,cutoff}}$ (ev)
HD122563	4528±42	0.66±0.12	-2.98±0.03	1.84±0.03	72	2.7	4620±59	1.21±0.19	-2.76±0.05	1.89±0.06	72	2.7
HD140283	5689±59	3.29±0.17	-2.72±0.04	2.09±0.14	96	2.0	5681±67	3.58±0.16	-2.64±0.05	2.17±0.16	96	2.0
Arcturus	4364±47	1.68±0.17	-0.64±0.05	1.76±0.02	70	0.0	4306±41	1.61±0.15	-0.63±0.04	1.79±0.02	70	0.0
GES Metal-Poor Stars (Hawkins et al. 2016)												
HD102200	6167±52	3.98±0.09	-1.26±0.02	0.62±0.09	33	2.5	6057±75	4.02±0.09	-1.26±0.04	0.98±0.28	37	4
HD106038	6108±51	4.05±0.07	-1.42±0.02	0.59±0.07	35	2.5	6124±60	4.29±0.08	-1.35±0.03	0.8±0.18	37	5
HD175305	5113±84	2.51±0.25	-1.47±0.05	1.61±0.2	45	2.5	5059±70	2.56±0.2	-1.43±0.04	1.61±0.17	45	6
HD201891	6036±86	4.23±0.15	-1.04±0.04	0.63±0.09	44	2.5	6047±81	4.33±0.14	-1.0±0.04	0.63±0.09	44	5
HD298986	6182±64	3.99±0.1	-1.42±0.03	0.61±0.08	37	2.5	6182±137	4.13±0.19	-1.35±0.07	1.0±0.33	39	5
CHARA Interferometry Stars (Karovicova et al. 2020, 2021a,b)												
HD131156	5538±46	4.55±0.1	-0.2±0.03	0.99±0.05	90	0.0	5501±47	4.53±0.1	-0.2±0.03	1.04±0.05	90	0.0
HD146233	5845±38	4.39±0.08	0.04±0.02	0.91±0.04	68	0.0	5788±39	4.37±0.08	0.04±0.03	0.96±0.04	68	0.0
HD186408	5842±46	4.33±0.1	0.03±0.03	1.1±0.03	96	0.0	5783±49	4.31±0.09	0.03±0.03	1.15±0.04	96	0.0
HD186427	5819±42	4.41±0.08	0.03±0.03	0.99±0.04	97	0.0	5771±45	4.41±0.09	0.03±0.03	1.05±0.04	97	0.0
HD190360	5538±33	4.37±0.06	0.13±0.02	0.8±0.05	49	0.0	5485±40	4.34±0.08	0.13±0.03	0.85±0.05	49	0.0
HD161797	5619±41	4.01±0.08	0.23±0.02	1.09±0.03	88	0.0	5536±30	3.99±0.06	0.3±0.02	0.93±0.03	85	0.0
HD207978	6493±24	3.99±0.05	-0.54±0.01	1.31±0.18	63	8	6407±41	3.96±0.14	-0.61±0.03	1.63±0.16	62	9
HD121370	6227±75	3.97±0.03	0.31±0.03	1.62±0.01	†	0.0	6120±64	3.91±0.06	0.3±0.02	1.62±0.04	†	0.0
HD175955	4608±48	2.69±0.14	0.07±0.04	1.03±0.03	86	14	4555±47	2.66±0.15	0.1±0.03	1.04±0.03	86	14
HD188512	5133±62	3.52±0.16	-0.22±0.04	0.83±0.07	34	7	5074±64	3.5±0.17	-0.22±0.04	0.92±0.07	34	7
HD103095	5114±91	4.37±0.32	-1.39±0.08	0.66±0.12	79	9	5215±95	4.66±0.21	-1.31±0.05	0.75±0.18	82	9
HD224930	5391±44	4.14±0.13	-0.9±0.03	0.79±0.08	76	11	5474±70	4.34±0.2	-0.82±0.04	0.7±0.12	81	11
GES-K2 Stars (Worley et al. 2020)												
22074607-1055493	4833±44	2.32±0.13	-1.03±0.03	1.22±0.02	138	16	4778±42	2.33±0.13	-0.99±0.03	1.23±0.02	138	16
22172723-1633039	4597±28	2.1±0.1	-0.82±0.02	1.32±0.01	136	15	4540±26	2.08±0.09	-0.81±0.02	1.36±0.01	136	15
22094505-1051031	4371±60	2.04±0.18	-0.5±0.05	1.57±0.03	134	13	4299±46	1.95±0.15	-0.49±0.05	1.6±0.04	133	13
22075605-1535081	4740±23	3.01±0.07	-0.01±0.01	1.17±0.01	151	17	4696±21	3.0±0.06	0.0±0.01	1.22±0.02	148	17
22072959-1530438	4957±19	3.32±0.05	-0.1±0.01	1.04±0.02	156	17	4892±18	3.27±0.05	-0.1±0.01	1.09±0.02	156	17
22391293-1502196	4840±20	3.08±0.06	-0.07±0.01	1.21±0.01	146	16	4776±20	3.02±0.06	-0.06±0.01	1.25±0.01	146	16

Table 3 continued

Table 3 (continued)

Star Name	LTE					NLTE						
	T_{eff} (K)	$\log g$ (cgs)	[Fe/H] (dex)	v_{mic} (km s $^{-1}$)	N_{FeI}	$\chi_{\text{FeI, cutoff}}$ (ev)	T_{eff} (K)	$\log g$ (cgs)	[Fe/H] (dex)	v_{mic} (km s $^{-1}$)	N_{FeII}	$\chi_{\text{FeI, cutoff}}$ (ev)
22390396-1500420	4630±30	2.98±0.09	-0.03±0.02	1.41±0.02	123	0.0	4586±28	2.95±0.09	-0.01±0.02	1.42±0.02	123	0.0
22035226-1457037	5015±15	3.31±0.04	-0.31±0.01	1.03±0.01	167	0.0	4950±15	3.26±0.04	-0.31±0.01	1.07±0.01	167	0.0
22071748-1455524	4706±19	2.71±0.06	-0.3±0.01	1.22±0.01	156	0.0	4646±19	2.68±0.07	-0.29±0.01	1.27±0.01	151	0.0
22033684-1449366	4834±19	2.59±0.06	-0.38±0.01	1.35±0.01	154	0.0	4742±17	2.5±0.06	-0.38±0.01	1.39±0.01	153	0.0
22072768-1440392	4601±25	2.88±0.08	0.04±0.02	1.22±0.02	131	0.0	4558±25	2.86±0.07	0.06±0.02	1.21±0.02	132	0.0
22254071-1431281	4893±28	2.6±0.1	-0.34±0.02	1.56±0.01	125	0.0	4812±26	2.55±0.1	-0.34±0.02	1.61±0.01	125	0.0
22243423-1430033	4531±34	2.65±0.11	0.18±0.03	1.5±0.02	94	0.0	4497±33	2.65±0.11	0.21±0.03	1.5±0.02	94	0.0
22235672-1428420	4755±17	2.85±0.06	-0.22±0.01	1.22±0.01	148	0.0	4697±17	2.82±0.06	-0.21±0.01	1.26±0.01	146	0.0
22235003-1422417	4753±31	3.35±0.08	0.3±0.02	1.23±0.03	119	0.0	4720±31	3.32±0.07	0.31±0.02	1.25±0.03	119	0.0
22175268-1344270	4773±18	2.57±0.07	-0.36±0.01	1.45±0.01	153	0.0	4702±17	2.52±0.07	-0.36±0.01	1.49±0.01	153	0.0
22250508-1341415	4741±20	2.77±0.07	-0.09±0.01	1.23±0.01	145	0.0	4662±19	2.69±0.06	-0.08±0.01	1.25±0.01	145	0.0
22174405-1338287	4792±17	2.81±0.06	-0.34±0.01	1.21±0.01	165	0.0	4728±17	2.76±0.06	-0.34±0.01	1.27±0.01	158	0.0
22185037-1257588	4528±25	2.69±0.08	-0.04±0.02	1.15±0.02	137	0.0	4491±25	2.68±0.08	-0.02±0.02	1.16±0.02	136	0.0
22204635-1245072	4804±23	3.35±0.06	0.19±0.01	1.02±0.02	143	0.0	4761±23	3.32±0.06	0.2±0.02	1.04±0.03	143	0.0
22195215-1234594	4707±26	2.72±0.08	-0.08±0.02	1.3±0.01	132	0.0	4653±24	2.7±0.08	-0.06±0.01	1.32±0.01	132	0.0
21563608-1202424	4792±19	3.13±0.06	-0.28±0.01	1.07±0.02	161	0.0	4738±19	3.08±0.06	-0.27±0.01	1.11±0.02	161	0.0
21590887-1159078	4678±26	2.71±0.08	-0.0±0.02	1.31±0.01	130	0.0	4623±25	2.68±0.08	0.02±0.02	1.32±0.01	130	0.0
22015504-1153022	4743±19	2.82±0.06	-0.25±0.01	1.29±0.01	155	0.0	4699±19	2.83±0.06	-0.23±0.01	1.33±0.01	150	0.0
22013369-1141245	4636±18	2.47±0.06	-0.43±0.01	1.31±0.01	152	0.0	4575±16	2.43±0.06	-0.41±0.01	1.34±0.01	153	0.0
22021848-1139147	4638±30	2.89±0.09	0.17±0.02	1.34±0.02	119	0.0	4597±28	2.87±0.09	0.19±0.02	1.35±0.02	119	0.0
22104061-1125284	4603±27	2.79±0.08	0.04±0.02	1.29±0.02	123	0.0	4559±26	2.77±0.08	0.06±0.02	1.29±0.02	123	0.0
22074730-1059405	4757±23	3.0±0.06	0.0±0.01	1.16±0.02	149	0.0	4712±21	3.0±0.06	0.01±0.01	1.22±0.02	146	0.0
22114557-0957433	4885±18	3.34±0.05	-0.16±0.01	1.03±0.02	153	0.0	4830±17	3.29±0.05	-0.16±0.01	1.06±0.02	153	0.0
22105372-0956597	4705±17	2.86±0.06	-0.37±0.01	1.09±0.01	158	0.0	4642±16	2.8±0.06	-0.37±0.01	1.17±0.01	148	0.0
22083624-0948555	4816±33	3.01±0.1	0.42±0.02	1.34±0.02	106	0.0	4769±33	3.0±0.09	0.45±0.02	1.34±0.02	106	0.0
22091180-0944335	4849±17	3.4±0.05	-0.24±0.01	0.9±0.02	159	0.0	4803±16	3.37±0.05	-0.23±0.01	0.93±0.02	159	0.0
22102197-0923157	4931±17	2.67±0.06	-0.2±0.01	1.32±0.01	143	0.0	4846±17	2.61±0.06	-0.2±0.01	1.37±0.01	142	0.0
22013945-0909229	4664±29	3.19±0.07	0.33±0.03	1.16±0.03	107	0.0	4634±29	3.17±0.07	0.34±0.03	1.17±0.03	107	0.0
22052550-0854435	4845±17	2.56±0.06	-0.32±0.01	1.49±0.01	156	0.0	4766±17	2.51±0.06	-0.33±0.01	1.53±0.01	155	0.0
22052114-0848002	4750±18	2.64±0.06	-0.36±0.01	1.22±0.01	158	0.0	4705±18	2.67±0.07	-0.35±0.01	1.31±0.01	145	0.0
22055148-0840028	4700±20	2.91±0.06	-0.27±0.01	1.19±0.01	162	0.0	4646±19	2.88±0.06	-0.27±0.01	1.24±0.01	158	0.0
22062074-0809079	4694±25	2.91±0.07	-0.01±0.02	1.23±0.02	136	0.0	4645±25	2.89±0.07	0.01±0.02	1.24±0.02	136	0.0

Table 3 continued

Table 3 (continued)

Star Name	LTE					NLTE							
	T_{eff} (K)	$\log g$ (cgs)	[Fe/H] (dex)	v_{mic} (km s $^{-1}$)	N_{FeI}	$\chi_{\text{FeI, cutoff}}$ (ev)	T_{eff} (K)	$\log g$ (cgs)	[Fe/H] (dex)	v_{mic} (km s $^{-1}$)	N_{FeII}	N_{FeI}	$\chi_{\text{FeI, cutoff}}$ (ev)
22291753-0806290	4664±19	2.9±0.06	-0.3±0.01	1.19±0.01	161	0.0	4615±17	2.87±0.06	-0.29±0.01	1.23±0.01	158	15	0.0
22122727-0719010	4428±27	2.46±0.1	-0.15±0.03	1.36±0.01	139	0.0	4389±27	2.46±0.09	-0.13±0.02	1.36±0.02	139	15	0.0
22292970-0713347	4833±19	2.64±0.06	-0.22±0.01	1.42±0.01	153	0.0	4757±17	2.59±0.06	-0.21±0.01	1.46±0.01	153	17	0.0
22130580-0658576	4594±27	2.78±0.09	-0.03±0.02	1.37±0.01	132	0.0	4550±26	2.76±0.08	-0.01±0.02	1.38±0.02	132	14	0.0
22092886-0617515	4731±21	3.02±0.06	-0.26±0.01	1.13±0.02	160	0.0	4693±22	3.02±0.06	-0.24±0.01	1.17±0.02	154	16	0.0
22153043-0617291	4942±16	2.5±0.06	-0.51±0.01	1.4±0.01	163	0.0	4850±17	2.44±0.06	-0.52±0.01	1.49±0.01	149	17	0.0
22092416-0610474	4789±24	2.7±0.08	-0.0±0.02	1.36±0.01	138	0.0	4726±24	2.67±0.08	0.03±0.01	1.38±0.01	139	16	0.0
22085850-0608204	4839±20	2.64±0.07	-0.32±0.01	1.36±0.01	148	0.0	4758±20	2.59±0.07	-0.32±0.01	1.4±0.01	147	10	0.0
22375413-0604257	4770±27	2.84±0.08	0.12±0.02	1.32±0.01	128	0.0	4712±26	2.81±0.08	0.13±0.02	1.36±0.01	129	16	0.0
22354169-0543252	4735±22	3.0±0.06	0.1±0.01	1.1±0.02	136	0.0	4693±21	3.0±0.06	0.13±0.01	1.11±0.02	139	15	0.0
22362945-0540124	4825±20	3.16±0.06	-0.17±0.01	1.17±0.02	150	0.0	4769±19	3.12±0.06	-0.17±0.01	1.21±0.02	150	15	0.0
22342769-0522505	4645±22	2.94±0.07	-0.1±0.01	1.19±0.02	153	0.0	4602±22	2.93±0.07	-0.09±0.01	1.21±0.02	151	15	0.0
22342069-0520353	4764±20	3.28±0.05	0.04±0.01	0.97±0.02	154	0.0	4720±19	3.24±0.05	0.05±0.01	0.99±0.02	154	16	0.0
22344800-0516214	4842±23	3.25±0.06	0.11±0.01	1.17±0.02	136	0.0	4790±21	3.21±0.06	0.12±0.01	1.19±0.02	136	17	0.0
<i>R</i> -Process Alliance Stars (Hansen et al. 2018)													
J03193531-3250433	6353±24	3.0±0.05	-2.97±0.01	2.81±0.15	11	2.7	6345±201	3.75±0.05	-2.77±0.1	2.8±0.15	11	5	2.7
J02401075-1416290	6041±116	4.4±0.19	-0.89±0.08	0.87±0.12	35	9	5991±107	4.34±0.18	-0.85±0.08	0.74±0.13	35	9	1.2
J00233067-1631428	5354±175	2.93±0.47	-2.53±0.12	2.12±0.2	28	13	5297±24	3.0±0.05	-2.45±0.03	1.7±0.17	28	13	2.7
J01334657-2727374	5216±151	2.46±0.42	-1.77±0.12	2.23±0.07	26	6	5221±147	2.65±0.35	-1.66±0.11	2.18±0.09	26	6	2.7
J00133067-1259594	4620±30	0.07±0.05	-2.78±0.03	1.82±0.07	36	9	4517±21	0.11±0.09	-2.73±0.03	1.8±0.06	36	9	2.7
J19215077-4452545	4659±23	0.1±0.07	-2.55±0.03	1.77±0.05	41	7	4561±32	0.13±0.11	-2.46±0.05	1.76±0.06	41	6	2.7
J23265258-0159248	4645±53	0.22±0.13	-3.13±0.04	1.94±0.08	32	15	4598±27	0.31±0.1	-3.0±0.03	1.88±0.09	32	15	2.7
J00405260-5122491	5547±59	4.01±0.22	-2.2±0.03	1.29±0.15	37	10	5495±75	3.93±0.23	-2.2±0.04	1.17±0.14	37	10	2.7
J15271353-2336177	6001±24	4.0±0.05	-2.16±0.01	1.64±0.08	48	13	6001±24	4.0±0.05	-2.11±0.02	1.82±0.13	48	13	2.7
J01530024-3417360	5171±65	2.96±0.13	-1.73±0.05	1.45±0.05	62	14	5116±93	2.96±0.18	-1.71±0.08	1.4±0.05	62	14	2.7
J16024498-1521016	5145±128	2.95±0.26	-1.99±0.1	1.69±0.05	44	13	5085±157	2.93±0.35	-1.99±0.14	1.69±0.05	44	13	2.7
J20514971-6158008	5221±145	2.97±0.29	-1.94±0.11	1.53±0.07	47	14	5187±134	3.01±0.29	-1.9±0.11	1.48±0.07	47	14	2.7
J16103106+1003055	5354±200	2.33±0.51	-2.44±0.13	1.68±0.21	32	3	5411±118	2.83±0.29	-2.26±0.13	1.5±0.09	32	3	1.2
J16184302-0630558	5293±103	1.14±0.29	-2.84±0.05	2.1±0.09	38	11	5339±114	2.1±0.39	-2.54±0.08	2.39±0.35	36	11	1.2
J21063474-4957500	5365±23	3.0±0.05	-2.89±0.02	1.53±0.12	33	9	5254±24	2.99±0.05	-2.88±0.02	1.26±0.09	33	9	2.7
J00021668-2453494	5140±160	1.81±0.48	-1.85±0.11	1.87±0.15	39	11	5185±145	2.24±0.39	-1.71±0.09	2.03±0.15	40	11	2.7
J02355867-6745520	4661±108	0.81±0.25	-1.7±0.08	2.09±0.12	30	10	4565±96	0.77±0.21	-1.66±0.07	2.14±0.08	31	10	2.7

Table 3 continued

Table 3 (continued)

Star Name	LTE					NLTE							
	T_{eff} (K)	$\log g$ (cgs)	[Fe/H] (dex)	v_{mic} (km s $^{-1}$)	N_{FeI}	$\chi_{\text{FeI, cutoff}}$ (ev)	T_{eff} (K)	$\log g$ (cgs)	[Fe/H] (dex)	v_{mic} (km s $^{-1}$)	N_{FeII}	N_{FeI}	$\chi_{\text{FeI, cutoff}}$ (ev)
J13164824-2743351	4821±95	1.78±0.3	-1.86±0.08	1.43±0.06	65	14	4806±91	1.96±0.27	-1.79±0.08	1.48±0.06	66	14	2.7
J14232679-2834200	4882±200	1.57±0.53	-2.19±0.17	1.39±0.08	45	9	4902±180	1.87±0.49	-2.08±0.15	1.43±0.07	46	9	2.7
J14301385-2317388	4352±51	0.67±0.13	-1.68±0.04	2.37±0.04	54	13	4298±39	0.65±0.11	-1.64±0.03	2.43±0.03	54	13	2.7
J15575183-0839549	4585±71	1.29±0.29	-1.82±0.07	1.92±0.06	55	16	4564±72	1.42±0.28	-1.74±0.07	1.96±0.04	56	16	2.7
J16080681-3215592	4531±27	0.49±0.18	-2.28±0.03	1.73±0.02	89	15	4460±26	0.63±0.14	-2.25±0.03	1.81±0.02	89	15	1.2
J17273886-5133298	5068±143	1.28±0.41	-1.85±0.08	2.07±0.16	52	13	5159±113	1.87±0.32	-1.67±0.06	2.28±0.13	52	13	2.7
J17334285-5121550	4864±153	0.99±0.37	-2.02±0.1	1.93±0.11	46	14	4891±167	1.22±0.44	-1.88±0.12	2.04±0.1	47	14	2.7
J18024226-4404426	4654±89	1.6±0.3	-1.65±0.08	1.94±0.04	47	8	4625±88	1.7±0.29	-1.57±0.08	1.97±0.05	48	8	2.7
J19014952-4844359	4602±26	1.06±0.11	-2.17±0.03	1.65±0.01	72	7	4549±27	1.14±0.11	-2.12±0.03	1.73±0.01	73	7	0.0
J19324858-5908019	4427±102	1.66±0.3	-2.13±0.08	1.72±0.08	29	7	4411±96	1.77±0.29	-2.09±0.08	1.75±0.09	29	7	2.7
J20144608-5635300	4828±115	1.36±0.39	-1.98±0.09	1.61±0.16	15	11	4773±130	1.53±0.41	-1.95±0.1	1.84±0.15	16	11	2.7
J22444701-5617540	4395±107	0.79±0.23	-2.09±0.08	1.8±0.09	22	6	4326±102	0.79±0.23	-2.09±0.08	1.95±0.08	22	6	2.7
J22492756-2238289	4768±105	1.09±0.31	-2.0±0.08	1.93±0.12	44	7	4782±102	1.38±0.29	-1.89±0.09	2.11±0.1	44	7	2.7
J22531984-2248555	4577±87	1.09±0.29	-2.11±0.07	1.58±0.07	52	14	4578±82	1.31±0.27	-2.03±0.07	1.66±0.07	53	14	2.7
J23362202-5607498	4459±106	0.81±0.24	-2.29±0.07	2.16±0.17	13	8	4495±109	0.9±0.27	-2.23±0.08	2.4±0.18	14	8	2.7
J00002259-1302275	4835±117	1.72±0.47	-2.46±0.1	2.4±0.33	44	5	4739±99	2.03±0.57	-2.52±0.09	2.52±0.3	43	5	0.0
J00021222-2241388	5180±137	2.03±0.43	-2.16±0.07	1.74±0.21	46	8	5164±113	2.34±0.37	-2.05±0.05	1.78±0.27	46	8	2.7
J00400685-4325183	4458±156	0.66±0.45	-2.65±0.13	2.06±0.14	25	7	4422±133	0.65±0.43	-2.55±0.13	2.04±0.14	25	8	2.7
J00453930-7457294	4727±37	1.49±0.17	-2.25±0.04	1.77±0.02	83	15	4684±35	1.65±0.16	-2.2±0.04	1.76±0.02	83	15	1.2
J01202234-5425582	5133±131	2.33±0.44	-2.11±0.08	1.45±0.16	48	9	5123±118	2.59±0.41	-2.01±0.08	1.39±0.19	48	9	2.7
J01293113-1600454	4678±133	1.09±0.41	-3.07±0.09	2.1±0.16	26	11	4800±134	1.76±0.35	-2.84±0.11	2.18±0.15	26	11	2.7
J01425422-5032488	5140±73	2.52±0.23	-2.18±0.06	1.66±0.06	49	15	5132±84	2.74±0.27	-2.08±0.06	1.6±0.11	49	15	2.7
J01430726-6445174	4582±66	0.51±0.25	-3.11±0.05	1.86±0.1	28	9	4563±76	0.9±0.27	-2.95±0.07	1.79±0.07	29	9	2.7
J01451951-2800583	4445±59	0.46±0.25	-2.89±0.05	1.63±0.03	31	12	4396±61	0.51±0.23	-2.8±0.06	1.61±0.03	31	12	2.7
J01490794-4911429	4691±72	0.77±0.24	-3.05±0.05	1.84±0.07	29	14	4845±81	1.61±0.22	-2.79±0.07	1.98±0.08	29	14	2.7
J02040793-3127556	4556±43	0.56±0.2	-3.17±0.04	2.1±0.06	67	16	4603±55	1.15±0.19	-3.01±0.07	2.24±0.07	66	16	1.2
J02165716-7547064	4531±64	0.48±0.26	-2.6±0.06	2.16±0.04	40	6	4537±65	0.7±0.24	-2.44±0.06	2.15±0.03	40	11	2.7
J02412152-1825376	4270±25	0.43±0.14	-2.3±0.02	1.52±0.03	64	9	4239±24	0.45±0.12	-2.31±0.02	1.71±0.02	63	10	1.2
J02441479-5158241	5223±120	2.28±0.4	-2.78±0.08	2.0±0.1	36	14	5201±79	2.7±0.26	-2.64±0.06	1.94±0.12	36	14	2.7
J02462013-1518419	5047±265	1.9±0.73	-2.77±0.2	2.69±0.22	15	9	5043±180	2.31±0.47	-2.61±0.13	2.62±0.24	15	9	2.7
J02500719-5145148	4575±37	0.96±0.18	-2.34±0.04	1.96±0.03	85	12	4527±38	1.11±0.16	-2.29±0.04	2.01±0.03	85	12	1.2
J03563703-5838281	4614±99	0.69±0.34	-2.78±0.08	2.1±0.06	30	9	4713±110	1.36±0.33	-2.55±0.1	2.07±0.06	30	9	2.7

Table 3 continued

Table 3 (continued)

Star Name	LTE					NLTE							
	T_{eff} (K)	$\log g$ (cgs)	[Fe/H] (dex)	v_{mic} (km s $^{-1}$)	N_{FeI}	$\chi_{\text{FeI, cutoff}}$ (ev)	T_{eff} (K)	$\log g$ (cgs)	[Fe/H] (dex)	v_{mic} (km s $^{-1}$)	N_{FeII}	$\chi_{\text{FeI, cutoff}}$ (ev)	
J04121388-1205050	4601±57	0.48±0.25	-2.82±0.06	2.21±0.05	22	1.2	4515±48	0.57±0.18	-2.78±0.06	2.33±0.05	22	7	1.2
J14033542-3335257	5040±127	1.97±0.32	-2.69±0.09	1.76±0.11	53	10	5116±102	2.48±0.28	-2.49±0.08	1.7±0.15	53	10	2.7
J14164084-2422000	4555±95	0.53±0.33	-2.78±0.07	1.77±0.06	38	16	4475±115	0.64±0.36	-2.7±0.1	1.77±0.05	38	16	2.7
J14325334-4125494	4729±127	1.51±0.36	-3.14±0.1	1.55±0.12	34	10	4791±113	1.95±0.31	-2.99±0.1	1.62±0.11	34	10	2.7
J14381119-2120085	4458±50	0.53±0.27	-2.44±0.04	1.9±0.03	47	14	4368±57	0.61±0.25	-2.41±0.05	1.91±0.03	48	13	2.7
J15260106-0911388	4697±119	0.72±0.38	-2.79±0.08	2.16±0.13	29	11	4784±128	1.37±0.36	-2.55±0.11	2.13±0.13	29	11	2.7
J15582962-1224344	5298±175	1.37±0.38	-2.58±0.09	2.63±0.22	44	16	5222±119	2.09±0.29	-2.39±0.09	2.73±0.21	44	16	2.7
J16095117-0941174	4620±58	0.57±0.24	-2.82±0.04	1.86±0.05	39	15	4767±70	1.39±0.18	-2.55±0.06	1.91±0.05	39	15	2.7
J17093199-6027271	4525±55	0.37±0.24	-2.49±0.06	2.12±0.05	53	8	4448±50	0.4±0.2	-2.41±0.06	2.11±0.03	53	8	1.2
J17094926-6239285	4611±123	0.88±0.43	-2.49±0.1	1.42±0.09	33	10	4712±118	1.47±0.33	-2.26±0.1	1.35±0.08	33	10	2.7
J17124284-5211479	4745±174	0.99±0.5	-2.77±0.13	1.24±0.12	26	10	4855±158	1.61±0.39	-2.54±0.13	1.28±0.1	26	10	2.7
J17225742-7123000	5019±113	2.36±0.33	-2.55±0.1	1.8±0.09	41	10	4998±97	2.58±0.28	-2.47±0.1	1.7±0.1	41	10	1.2
J17255680-6603395	4666±66	0.49±0.27	-2.66±0.05	2.13±0.05	35	12	4671±77	0.99±0.23	-2.5±0.07	2.05±0.05	35	12	2.7
J17285930-7427532	4760±136	1.1±0.57	-2.18±0.09	1.41±0.13	38	8	4773±95	1.44±0.42	-2.07±0.06	1.45±0.13	38	8	2.7
J17400682-6102129	4594±91	0.93±0.33	-2.52±0.07	1.8±0.05	43	12	4625±96	1.32±0.29	-2.37±0.08	1.8±0.04	43	12	2.7
J17435113-5359333	5198±147	1.85±0.43	-2.28±0.07	2.13±0.24	58	14	5203±121	2.37±0.35	-2.12±0.07	2.13±0.23	58	12	2.7
J18121045-4934495	4526±79	0.6±0.29	-3.03±0.06	2.19±0.09	27	9	4657±89	1.31±0.27	-2.78±0.08	2.2±0.08	27	9	2.7
J18285086-3434203	4706±93	1.16±0.3	-2.4±0.07	1.62±0.07	60	14	4735±88	1.51±0.25	-2.25±0.08	1.64±0.07	60	14	2.7
J18294122-4504000	4572±92	0.71±0.34	-2.67±0.08	1.8±0.05	38	7	4624±96	1.2±0.29	-2.48±0.1	1.73±0.05	38	7	2.7
J18362318-6428124	4700±90	1.17±0.28	-2.77±0.07	1.78±0.07	34	13	4823±91	1.77±0.25	-2.54±0.07	1.79±0.06	34	13	2.7
J18363613-7136597	4574±150	0.56±0.43	-2.65±0.12	2.1±0.1	41	9	4556±91	0.58±0.32	-2.46±0.09	2.02±0.05	41	13	2.7
J18562774-7251331	4641±65	0.48±0.32	-2.32±0.06	1.74±0.05	38	4	4538±88	0.56±0.33	-2.26±0.09	1.75±0.03	38	4	2.7
J19161821-5544454	4449±21	0.23±0.17	-2.4±0.02	1.99±0.09	32	10	4377±22	0.3±0.18	-2.38±0.03	2.12±0.08	32	10	2.7
J19172402-4211240	4568±88	0.59±0.32	-2.83±0.07	1.96±0.08	53	13	4681±109	1.25±0.3	-2.59±0.1	1.99±0.08	53	13	2.7
J19173310-6628545	4608±160	0.89±0.52	-2.81±0.12	2.53±0.13	19	9	4668±164	1.35±0.47	-2.63±0.14	2.49±0.1	19	9	2.7
J19202070-6627202	4426±31	0.59±0.21	-2.4±0.03	1.45±0.03	81	11	4451±38	1.04±0.16	-2.34±0.04	1.6±0.04	78	11	1.2
J19232518-5833410	5029±209	1.87±0.69	-2.17±0.13	2.05±0.36	36	7	5039±155	2.21±0.57	-2.06±0.09	2.14±0.35	36	7	2.7
J19345497-5751400	4841±204	2.09±0.66	-2.33±0.17	2.41±0.14	11	5	4841±190	2.4±0.67	-2.23±0.15	2.29±0.12	11	5	2.7
J19494025-5424113	4648±129	0.87±0.41	-2.83±0.1	2.09±0.1	25	9	4733±123	1.47±0.34	-2.63±0.11	2.08±0.06	25	9	2.7
J19534978-5940001	4708±45	0.49±0.19	-2.83±0.04	2.46±0.05	41	10	4672±62	0.96±0.21	-2.65±0.08	2.24±0.05	43	10	1.2
J19594558-2549075	4523±72	0.46±0.29	-2.5±0.05	2.15±0.05	42	15	4442±81	0.52±0.26	-2.45±0.07	2.16±0.05	42	15	2.7
J20093393-3410273	4410±39	1.64±0.15	-2.19±0.02	2.18±0.08	62	7	4312±20	1.77±0.18	-2.22±0.02	2.19±0.07	62	7	1.2

Table 3 continued

Table 3 (continued)

Star Name	LTE				NLTE				$\chi_{\text{FeI,cutoff}}$ (ev)	$\chi_{\text{FeI,cutoff}}$ (ev)			
	T_{eff} (K)	$\log g$ (cgs)	[Fe/H] (dex)	v_{mic} (km s $^{-1}$)	N_{FeI}	$\chi_{\text{FeI,cutoff}}$ (ev)	T_{eff} (K)	$\log g$ (cgs)			[Fe/H] (dex)	v_{mic} (km s $^{-1}$)	N_{FeII}
J20165357–0503592	4546±105	0.6±0.33	−2.96±0.09	2.11±0.11	35	7	4639±127	1.21±0.36	−2.74±0.13	2.13±0.09	35	7	2.7
J20303339–2519500	4378±17	0.06±0.05	−2.29±0.02	1.75±0.03	65	16	4312±23	0.12±0.11	−2.24±0.02	1.83±0.05	65	16	2.7
J20313531–3127319	4658±107	0.7±0.34	−2.72±0.08	1.96±0.09	28	10	4759±125	1.36±0.33	−2.49±0.11	1.98±0.11	28	10	2.7
J20445584–2250597	4330±44	0.5±0.23	−2.49±0.03	2.03±0.03	54	14	4266±51	0.5±0.24	−2.49±0.04	2.21±0.04	55	14	2.7
J20492765–5124440	4503±67	0.55±0.28	−2.49±0.06	1.81±0.04	38	9	4492±76	0.87±0.27	−2.39±0.07	1.83±0.03	38	9	2.7
J20542346–0033097	4414±57	0.52±0.27	−2.87±0.05	2.53±0.06	36	13	4402±78	0.76±0.27	−2.77±0.08	2.49±0.05	37	13	2.7
J20560913–1331176	4615±53	0.98±0.2	−2.5±0.04	1.65±0.02	58	17	4668±54	1.41±0.16	−2.34±0.05	1.63±0.02	58	17	2.7
J21023752–5316132	5198±289	2.4±0.94	−2.32±0.22	1.36±0.36	29	9	5178±162	2.6±0.5	−2.22±0.08	1.22±0.33	29	9	2.7
J21064294–6828266	4830±255	1.7±0.76	−3.1±0.21	2.76±0.17	11	9	4843±251	2.08±0.74	−2.97±0.21	2.79±0.15	11	9	2.7
J21091825–1310062	4746±106	0.97±0.35	−2.51±0.08	1.79±0.06	46	18	4820±103	1.53±0.29	−2.31±0.09	1.8±0.05	46	18	2.7
J21095804–0945400	4493±77	0.68±0.3	−2.85±0.06	1.79±0.07	19	7	4555±83	1.15±0.27	−2.66±0.08	1.77±0.05	19	7	2.7
J21141350–5726363	4515±67	0.51±0.24	−2.95±0.06	1.94±0.05	57	7	4590±79	1.12±0.23	−2.74±0.09	1.96±0.05	57	7	2.7
J21152551–1503309	4505±72	0.52±0.33	−2.32±0.05	1.77±0.06	38	14	4458±82	0.69±0.3	−2.29±0.07	1.86±0.03	37	10	2.7
J21162185–0213420	4418±25	0.08±0.06	−2.33±0.03	1.48±0.04	41	7	4234±43	0.45±0.25	−2.44±0.05	1.86±0.05	37	2	2.7
J21224590–4641030	4743±123	1.11±0.41	−2.9±0.09	2.23±0.13	24	11	4842±125	1.75±0.33	−2.68±0.11	2.25±0.12	24	11	2.7
J21262525–2144243	4362±61	0.57±0.26	−2.93±0.06	1.84±0.04	52	10	4400±66	0.96±0.23	−2.78±0.07	1.82±0.04	52	10	2.7
J21291592–4236219	4602±104	0.82±0.38	−2.63±0.08	2.08±0.07	43	14	4673±110	1.34±0.32	−2.44±0.1	2.05±0.06	43	14	2.7
J21370807–0927347	4507±119	0.72±0.5	−2.53±0.1	1.86±0.09	34	8	4364±109	0.63±0.37	−2.52±0.11	1.84±0.08	36	8	2.7
J21513595–0543398	4489±71	0.44±0.24	−2.59±0.06	2.02±0.04	42	14	4412±52	0.49±0.2	−2.55±0.05	2.08±0.05	42	14	2.7
J22021636–0536483	4695±58	0.74±0.25	−2.76±0.05	2.03±0.07	42	10	4731±68	1.31±0.24	−2.57±0.08	2.06±0.05	42	10	1.2
J22163596+0246171	4759±114	1.41±0.34	−2.51±0.1	1.49±0.06	49	7	4761±104	1.7±0.28	−2.39±0.1	1.44±0.05	49	7	2.7
J22595884–1554182	4552±101	0.57±0.33	−2.73±0.08	2.14±0.05	44	12	4543±118	0.87±0.37	−2.57±0.11	2.05±0.05	44	12	2.7
J23022289–6833233	5232±162	2.23±0.51	−2.52±0.11	1.79±0.17	39	7	5227±144	2.72±0.49	−2.39±0.1	1.82±0.29	39	7	2.7
J23044914–4243477	4670±98	1.58±0.32	−2.48±0.09	0.79±0.07	26	12	4634±91	1.68±0.27	−2.43±0.09	0.77±0.07	26	12	1.2
J23130003–4507066	4589±83	0.57±0.32	−2.68±0.06	1.79±0.06	35	13	4675±100	1.17±0.31	−2.46±0.09	1.79±0.07	35	13	2.7
J23310716–0223301	4873±228	1.08±0.64	−2.5±0.16	2.06±0.18	12	3	4938±201	1.68±0.56	−2.28±0.16	2.06±0.2	12	3	2.7

NOTE—

† For HD121370, parameters are obtained with the average of runs inputting 3 different EW line lists: EPINARBO in Heiter et al. (2015), BOLOGNA in Heiter et al. (2015) and Takeda et al. (2005). In LTE, there are $N_{\text{FeI}}=79$, 121, 46, $N_{\text{FeII}}=6$, 9, 4 lines in these three line list respectively; In NLTE, $N_{\text{FeI}}=79$, 121, 47, $N_{\text{FeII}}=6$, 9, 4

(This table is available in machine-readable form.)

REFERENCES

- Ahumada, R., Prieto, C. A., Almeida, A., et al. 2020, *ApJS*, 249, 3, doi: [10.3847/1538-4365/ab929e](https://doi.org/10.3847/1538-4365/ab929e)
- Amarsi, A. M., Lind, K., Asplund, M., Barklem, P. S., & Collet, R. 2016, *MNRAS*, 463, 1518, doi: [10.1093/mnras/stw2077](https://doi.org/10.1093/mnras/stw2077)
- Amarsi, A. M., Lind, K., Osorio, Y., et al. 2020, *A&A*, 642, A62, doi: [10.1051/0004-6361/202038650](https://doi.org/10.1051/0004-6361/202038650)
- Asplund, M. 2005, *ARA&A*, 43, 481, doi: [10.1146/annurev.astro.42.053102.134001](https://doi.org/10.1146/annurev.astro.42.053102.134001)
- Asplund, M., Grevesse, N., Sauval, A. J., & Scott, P. 2009, *ARA&A*, 47, 481, doi: [10.1146/annurev.astro.46.060407.145222](https://doi.org/10.1146/annurev.astro.46.060407.145222)
- Astropy Collaboration, Robitaille, T. P., Tollerud, E. J., et al. 2013, *A&A*, 558, A33, doi: [10.1051/0004-6361/201322068](https://doi.org/10.1051/0004-6361/201322068)
- Astropy Collaboration, Price-Whelan, A. M., Sipócz, B. M., et al. 2018, *AJ*, 156, 123, doi: [10.3847/1538-3881/aabc4f](https://doi.org/10.3847/1538-3881/aabc4f)
- Audouze, J., & Tinsley, B. M. 1976, *ARA&A*, 14, 43, doi: [10.1146/annurev.aa.14.090176.000355](https://doi.org/10.1146/annurev.aa.14.090176.000355)
- Barklem, P. S. 2018, *A&A*, 612, A90, doi: [10.1051/0004-6361/201732365](https://doi.org/10.1051/0004-6361/201732365)
- Bergemann, M., Lind, K., Collet, R., Magic, Z., & Asplund, M. 2012, *MNRAS*, 427, 27, doi: [10.1111/j.1365-2966.2012.21687.x](https://doi.org/10.1111/j.1365-2966.2012.21687.x)
- Bernstein, R., Shtetman, S. A., Gunnels, S. M., Mochnecki, S., & Athey, A. E. 2003, in *Instrument Design and Performance for Optical/Infrared Ground-based Telescopes*, ed. M. Iye & A. F. M. Moorwood, Vol. 4841, International Society for Optics and Photonics (SPIE), 1694 – 1704, doi: [10.1117/12.461502](https://doi.org/10.1117/12.461502)
- Boeche, C., & Grebel, E. K. 2016, *A&A*, 587, A2, doi: [10.1051/0004-6361/201526758](https://doi.org/10.1051/0004-6361/201526758)
- Brodtkorb, P. A., & D’Errico, J. 2015, *numdifftools* 0.9.11, <https://github.com/pbrod/numdifftools>
- Buitinck, L., Louppe, G., Blondel, M., et al. 2013, in *ECML PKDD Workshop: Languages for Data Mining and Machine Learning*, 108–122
- Cantat-Gaudin, T., Donati, P., Pancino, E., et al. 2014, *A&A*, 562, A10, doi: [10.1051/0004-6361/201322533](https://doi.org/10.1051/0004-6361/201322533)
- Casagrande, L., Ramírez, I., Meléndez, J., Bessell, M., & Asplund, M. 2010, *A&A*, 512, A54, doi: [10.1051/0004-6361/200913204](https://doi.org/10.1051/0004-6361/200913204)
- Casagrande, L., Schönrich, R., Asplund, M., et al. 2011, *A&A*, 530, A138, doi: [10.1051/0004-6361/201016276](https://doi.org/10.1051/0004-6361/201016276)
- Collette, A. 2013, *Python and HDF5* (O’Reilly)
- Creevey, O., Grundahl, F., Thévenin, F., et al. 2019, *A&A*, 625, A33, doi: [10.1051/0004-6361/201834721](https://doi.org/10.1051/0004-6361/201834721)
- Creevey, O. L., Thévenin, F., Boyajian, T. S., et al. 2012, *A&A*, 545, A17, doi: [10.1051/0004-6361/201219651](https://doi.org/10.1051/0004-6361/201219651)
- Creevey, O. L., Thévenin, F., Berio, P., et al. 2015, *A&A*, 575, A26, doi: [10.1051/0004-6361/201424310](https://doi.org/10.1051/0004-6361/201424310)
- Cui, X.-Q., Zhao, Y.-H., Chu, Y.-Q., et al. 2012, *Research in Astronomy and Astrophysics*, 12, 1197, doi: [10.1088/1674-4527/12/9/003](https://doi.org/10.1088/1674-4527/12/9/003)
- Dalton, G., Trager, S., Abrams, D. C., et al. 2016, in *Society of Photo-Optical Instrumentation Engineers (SPIE) Conference Series*, Vol. 9908, *Ground-based and Airborne Instrumentation for Astronomy VI*, ed. C. J. Evans, L. Simard, & H. Takami, 99081G, doi: [10.1117/12.2231078](https://doi.org/10.1117/12.2231078)
- de Jong, R. S., Agertz, O., Berbel, A. A., et al. 2019, *The Messenger*, 175, 3, doi: [10.18727/0722-6691/5117](https://doi.org/10.18727/0722-6691/5117)
- De Silva, G. M., Freeman, K. C., Bland-Hawthorn, J., et al. 2015, *MNRAS*, 449, 2604, doi: [10.1093/mnras/stv327](https://doi.org/10.1093/mnras/stv327)
- Deng, L.-C., Newberg, H. J., Liu, C., et al. 2012, *Research in Astronomy and Astrophysics*, 12, 735, doi: [10.1088/1674-4527/12/7/003](https://doi.org/10.1088/1674-4527/12/7/003)
- Dotter, A., Chaboyer, B., Jevremović, D., et al. 2008, *ApJS*, 178, 89, doi: [10.1086/589654](https://doi.org/10.1086/589654)
- Ezzeddine, R., Frebel, A., & Plez, B. 2017, *ApJ*, 847, 142, doi: [10.3847/1538-4357/aa8875](https://doi.org/10.3847/1538-4357/aa8875)
- Ezzeddine, R., Merle, T., & Plez, B. 2016, *Astronomische Nachrichten*, 337, 850, doi: [10.1002/asna.201612384](https://doi.org/10.1002/asna.201612384)
- Ezzeddine, R., Rasmussen, K., Frebel, A., et al. 2020, *ApJ*, 898, 150, doi: [10.3847/1538-4357/ab9d1a](https://doi.org/10.3847/1538-4357/ab9d1a)
- Foreman-Mackey, D. 2016, *The Journal of Open Source Software*, 1, 24, doi: [10.21105/joss.00024](https://doi.org/10.21105/joss.00024)
- Frebel, A., Casey, A. R., Jacobson, H. R., & Yu, Q. 2013, *ApJ*, 769, 57, doi: [10.1088/0004-637X/769/1/57](https://doi.org/10.1088/0004-637X/769/1/57)

- García Pérez, A. E., Allende Prieto, C., Holtzman, J. A., et al. 2016, *AJ*, 151, 144, doi: [10.3847/0004-6256/151/6/144](https://doi.org/10.3847/0004-6256/151/6/144)
- Geman, S., & Geman, D. 1984, *IEEE Transactions on Pattern Analysis and Machine Intelligence*, PAMI-6, 721, doi: [10.1109/TPAMI.1984.4767596](https://doi.org/10.1109/TPAMI.1984.4767596)
- Giribaldi, R. E., da Silva, A. R., Smiljanic, R., & Cornejo Espinoza, D. 2021, *A&A*, 650, A194, doi: [10.1051/0004-6361/202140751](https://doi.org/10.1051/0004-6361/202140751)
- Griffin, R. E. M., & Lynas-Gray, A. E. 1999, *AJ*, 117, 2998, doi: [10.1086/300878](https://doi.org/10.1086/300878)
- Gustafsson, B., Bell, R. A., Eriksson, K., & Nordlund, A. 1975, *A&A*, 42, 407
- Gustafsson, B., Edvardsson, B., Eriksson, K., et al. 2008, *A&A*, 486, 951, doi: [10.1051/0004-6361:200809724](https://doi.org/10.1051/0004-6361:200809724)
- Hansen, T. T., Holmbeck, E. M., Beers, T. C., et al. 2018, *ApJ*, 858, 92, doi: [10.3847/1538-4357/aabacc](https://doi.org/10.3847/1538-4357/aabacc)
- Harris, C. R., Millman, K. J., van der Walt, S. J., et al. 2020, *Nature*, 585, 357, doi: [10.1038/s41586-020-2649-2](https://doi.org/10.1038/s41586-020-2649-2)
- Hauschildt, P. H., Baron, E., & Allard, F. 1997, *ApJ*, 483, 390, doi: [10.1086/304233](https://doi.org/10.1086/304233)
- Hawkins, K., Jofré, P., Heiter, U., et al. 2016, *A&A*, 592, A70, doi: [10.1051/0004-6361/201628268](https://doi.org/10.1051/0004-6361/201628268)
- Heiter, U., Jofré, P., Gustafsson, B., et al. 2015, *A&A*, 582, A49, doi: [10.1051/0004-6361/201526319](https://doi.org/10.1051/0004-6361/201526319)
- Heiter, U., Lind, K., Bergemann, M., et al. 2021, *A&A*, 645, A106, doi: [10.1051/0004-6361/201936291](https://doi.org/10.1051/0004-6361/201936291)
- Holmbeck, E. M., Hansen, T. T., Beers, T. C., et al. 2020, *ApJS*, 249, 30, doi: [10.3847/1538-4365/ab9c19](https://doi.org/10.3847/1538-4365/ab9c19)
- Hubeny, I., & Mihalas, D. 2014, *Theory of Stellar Atmospheres*
- Hunter, J. D. 2007, *Computing in Science & Engineering*, 9, 90, doi: [10.1109/MCSE.2007.55](https://doi.org/10.1109/MCSE.2007.55)
- Jofré, P., Heiter, U., & Soubiran, C. 2019, *ARA&A*, 57, 571, doi: [10.1146/annurev-astro-091918-104509](https://doi.org/10.1146/annurev-astro-091918-104509)
- Jofré, P., Heiter, U., Soubiran, C., et al. 2014, *A&A*, 564, A133, doi: [10.1051/0004-6361/201322440](https://doi.org/10.1051/0004-6361/201322440)
- Karovicova, I., White, T. R., Nordlander, T., et al. 2021a, arXiv e-prints, arXiv:2109.06203, <https://arxiv.org/abs/2109.06203>
- . 2021b, arXiv e-prints, arXiv:2109.13258, <https://arxiv.org/abs/2109.13258>
- . 2020, *A&A*, 640, A25, doi: [10.1051/0004-6361/202037590](https://doi.org/10.1051/0004-6361/202037590)
- . 2018, *MNRAS*, 475, L81, doi: [10.1093/mnrasl/sly010](https://doi.org/10.1093/mnrasl/sly010)
- Kobayashi, C., Umeda, H., Nomoto, K., Tominaga, N., & Ohkubo, T. 2006, *ApJ*, 653, 1145, doi: [10.1086/508914](https://doi.org/10.1086/508914)
- Kollmeier, J. A., Zasowski, G., Rix, H.-W., et al. 2017, arXiv e-prints, arXiv:1711.03234, <https://arxiv.org/abs/1711.03234>
- Lacour, S., Meimon, S., Thiébaud, E., et al. 2008, *A&A*, 485, 561, doi: [10.1051/0004-6361:200809611](https://doi.org/10.1051/0004-6361:200809611)
- Lind, K., Bergemann, M., & Asplund, M. 2012, *MNRAS*, 427, 50, doi: [10.1111/j.1365-2966.2012.21686.x](https://doi.org/10.1111/j.1365-2966.2012.21686.x)
- Linsky, J. L. 2017, *ARA&A*, 55, 159, doi: [10.1146/annurev-astro-091916-055327](https://doi.org/10.1146/annurev-astro-091916-055327)
- Liu, C., Fu, J., Shi, J., et al. 2020, arXiv e-prints, arXiv:2005.07210, <https://arxiv.org/abs/2005.07210>
- Magrini, L., Randich, S., Friel, E., et al. 2013, *A&A*, 558, A38, doi: [10.1051/0004-6361/201321844](https://doi.org/10.1051/0004-6361/201321844)
- Mashonkina, L., Gehren, T., Shi, J. R., Korn, A. J., & Grupp, F. 2011, *A&A*, 528, A87, doi: [10.1051/0004-6361/201015336](https://doi.org/10.1051/0004-6361/201015336)
- Mashonkina, L., Jablonka, P., Sitnova, T., Pakhomov, Y., & North, P. 2017, *A&A*, 608, A89, doi: [10.1051/0004-6361/201731582](https://doi.org/10.1051/0004-6361/201731582)
- McWilliam, A. 1997, *ARA&A*, 35, 503, doi: [10.1146/annurev.astro.35.1.503](https://doi.org/10.1146/annurev.astro.35.1.503)
- Metropolis, N., & Ulam, S. 1949, *Journal of the American Statistical Association*, 44, 335, doi: [10.1080/01621459.1949.10483310](https://doi.org/10.1080/01621459.1949.10483310)
- Meurer, A., Smith, C. P., Paprocki, M., et al. 2017, *PeerJ Computer Science*, 3, e103, doi: [10.7717/peerj-cs.103](https://doi.org/10.7717/peerj-cs.103)
- Miesch, M. S., & Toomre, J. 2009, *Annual Review of Fluid Mechanics*, 41, 317, doi: [10.1146/annurev.fluid.010908.165215](https://doi.org/10.1146/annurev.fluid.010908.165215)
- Miglio, A., Chiappini, C., Mosser, B., et al. 2017, *Astronomische Nachrichten*, 338, 644, doi: [10.1002/asna.201713385](https://doi.org/10.1002/asna.201713385)
- Mihalas, D., & Athay, R. G. 1973, *ARA&A*, 11, 187, doi: [10.1146/annurev.aa.11.090173.001155](https://doi.org/10.1146/annurev.aa.11.090173.001155)
- Morel, T., Miglio, A., Lagarde, N., et al. 2014, *VizieR Online Data Catalog*, J/A+A/564/A119

- Mucciarelli, A., Pancino, E., Lovisi, L., Ferraro, F. R., & Lapenna, E. 2013, *ApJ*, 766, 78, doi: [10.1088/0004-637X/766/2/78](https://doi.org/10.1088/0004-637X/766/2/78)
- Neal, R. M. 2003, *The Annals of Statistics*, 31, 705, doi: [10.1214/aos/1056562461](https://doi.org/10.1214/aos/1056562461)
- Osorio, Y., Barklem, P. S., Lind, K., et al. 2015, *A&A*, 579, A53, doi: [10.1051/0004-6361/201525846](https://doi.org/10.1051/0004-6361/201525846)
- pandas development team, T. 2020, pandas-dev/pandas: Pandas, latest, Zenodo, doi: [10.5281/zenodo.3509134](https://doi.org/10.5281/zenodo.3509134)
- Piskunov, N., & Valenti, J. A. 2017, *A&A*, 597, A16, doi: [10.1051/0004-6361/201629124](https://doi.org/10.1051/0004-6361/201629124)
- Quirrenbach, A., Mozurkewich, D., Buscher, D. F., Hummel, C. A., & Armstrong, J. T. 1996, *A&A*, 312, 160
- Ramírez, I., & Allende Prieto, C. 2011, *ApJ*, 743, 135, doi: [10.1088/0004-637X/743/2/135](https://doi.org/10.1088/0004-637X/743/2/135)
- Recio-Blanco, A., Bijaoui, A., & de Laverny, P. 2006, *MNRAS*, 370, 141, doi: [10.1111/j.1365-2966.2006.10455.x](https://doi.org/10.1111/j.1365-2966.2006.10455.x)
- Roederer, I. U., Sakari, C. M., Placco, V. M., et al. 2018, *The Astrophysical Journal*, 865, 129, doi: [10.3847/1538-4357/aadd92](https://doi.org/10.3847/1538-4357/aadd92)
- Rybicki, G. B., & Hummer, D. G. 1991, *A&A*, 245, 171
- Sakari, C. M., Placco, V. M., Farrell, E. M., et al. 2018, *ApJ*, 868, 110, doi: [10.3847/1538-4357/aae9df](https://doi.org/10.3847/1538-4357/aae9df)
- Salvatier, J., Wiecki, T. V., & Fonnesbeck, C. 2016, *PeerJ Computer Science*, 2, e55
- Sbordone, L., Caffau, E., Bonifacio, P., & Duffau, S. 2014, *A&A*, 564, A109, doi: [10.1051/0004-6361/201322430](https://doi.org/10.1051/0004-6361/201322430)
- Sousa, S. G., Santos, N. C., Adibekyan, V., Delgado-Mena, E., & Israelian, G. 2015, *A&A*, 577, A67, doi: [10.1051/0004-6361/201425463](https://doi.org/10.1051/0004-6361/201425463)
- Steinmetz, M., Matijević, G., Enke, H., et al. 2020, *AJ*, 160, 82, doi: [10.3847/1538-3881/ab9ab9](https://doi.org/10.3847/1538-3881/ab9ab9)
- Storn, R., & Price, K. 1996, in *Proceedings of IEEE International Conference on Evolutionary Computation*, 842–844, doi: [10.1109/ICEC.1996.542711](https://doi.org/10.1109/ICEC.1996.542711)
- Taberner, H. M., Marfil, E., Montes, D., & González Hernández, J. I. 2019, *A&A*, 628, A131, doi: [10.1051/0004-6361/201935465](https://doi.org/10.1051/0004-6361/201935465)
- Takeda, Y., Sato, B., Kambe, E., et al. 2005, *PASJ*, 57, 109, doi: [10.1093/pasj/57.1.109](https://doi.org/10.1093/pasj/57.1.109)
- Takeda, Y., & Tajitsu, A. 2015, *MNRAS*, 450, 397, doi: [10.1093/mnras/stv682](https://doi.org/10.1093/mnras/stv682)
- Team, T. T. D., Al-Rfou, R., Alain, G., et al. 2016, arXiv preprint arXiv:1605.02688
- Tsantaki, M., & Andreasen, D. 2021, in *The 20.5th Cambridge Workshop on Cool Stars, Stellar Systems, and the Sun (CS20.5)*, Cambridge Workshop on Cool Stars, Stellar Systems, and the Sun, 172, doi: [10.5281/zenodo.4565462](https://doi.org/10.5281/zenodo.4565462)
- Tsantaki, M., Santos, N. C., Sousa, S. G., et al. 2019, *MNRAS*, 485, 2772, doi: [10.1093/mnras/stz578](https://doi.org/10.1093/mnras/stz578)
- van der Walt, S., Colbert, S. C., & Varoquaux, G. 2011, *Computing in Science and Engineering*, 13, 22, doi: [10.1109/MCSE.2011.37](https://doi.org/10.1109/MCSE.2011.37)
- Vanderburg, A., Plavchan, P., Johnson, J. A., et al. 2016, *MNRAS*, 459, 3565, doi: [10.1093/mnras/stw863](https://doi.org/10.1093/mnras/stw863)
- Virtanen, P., Gommers, R., Oliphant, T. E., et al. 2020, *Nature Methods*, 17, 261, doi: [10.1038/s41592-019-0686-2](https://doi.org/10.1038/s41592-019-0686-2)
- Wehrhahn, A. 2021, in *The 20.5th Cambridge Workshop on Cool Stars, Stellar Systems, and the Sun (CS20.5)*, Cambridge Workshop on Cool Stars, Stellar Systems, and the Sun, 1, doi: [10.5281/zenodo.4537913](https://doi.org/10.5281/zenodo.4537913)
- Wijbenga, J. W., & Zwaan, C. 1972, *SoPh*, 23, 265, doi: [10.1007/BF00148089](https://doi.org/10.1007/BF00148089)
- Worley, C. C., Jofré, P., Rendle, B., et al. 2020, *A&A*, 643, A83, doi: [10.1051/0004-6361/201936726](https://doi.org/10.1051/0004-6361/201936726)
- Zhao, G., Zhao, Y., Chu, Y., Jing, Y., & Deng, L. 2012, arXiv e-prints, arXiv:1206.3569. <https://arxiv.org/abs/1206.3569>